



The Australian National University
Centre For Gravitational Physics

Coating-Free Mirrors for Ultra-Sensitive Interferometry

Jeff Cumpston

A thesis submitted for the degree of
Bachelor of Science (hons)
at
The Australian National University

Submitted
29th of May, 2006

Declaration

This thesis is an account of research undertaken between July 2005 and May 2006 at The Department of Physics, Faculty of Science, The Australian National University, Canberra, Australia.

Except where acknowledged in the customary manner, the material presented in this thesis, along with the design of the coating-free mirror, is, to the best of my knowledge, original and has not been submitted in whole or part for a degree in any other university.

Important contributions made by others are appropriately referenced in the text.

Jeff Cumpston
29th May 2006

Acknowledgements

First of all I would like to my supervisors, Dr. Stefan Gößler and Professor David McClelland.

I thank David for his guidance and support; for always making himself available to review my work and to provide advice, especially at the times I needed it the most. I thank him most of all for providing me with the opportunity to work in the group. I have learnt so much since I started here; about experimental optics, but also about the greater world of physics outside of undergraduate coursework.

My direct supervisor, Stefan, has left me in awe of his selflessness. I have been amazed at the amount of personal time and effort he has invested in helping me to obtain the best results possible. I will be forever grateful for his encouragement and friendship during this time, and also for his strict demands on attention to detail in document writing, which has never been one of my strong points.

I am grateful to Kirk McKenzie for always taking the time to answer my questions, and for the loan of the amplitude modulator, without which the experimental data obtained in this project may have been severely limited. I thank Conor Mow-Lowry for interesting discussions about details of the project, and for introducing me to Magical Trevor.

Thanks to Mal Gray and James Dickson for designing and building the electronics used in this project.

Thanks to my other colleagues Bram Slagmolen, David Rabeling, Glenn de Vine, Lee Pedersen, Theo Karner, Jong Chow, Ben Sheard, Adam Mullavey for creating an excellent working environment. It's been fun, and I look forward to working more with you all in the future.

For proof reading of this document I thank David McClelland, Stefan Gößler, Kirk McKenzie.

During the course of my honours, my parents, Mike and Pauline, have always been there to help me out with advice, and never failed to call once a week to make sure I was doing all right. For this I thank them.

Finally, thank you Tess, for your patience and love during this incredibly busy time.

Abstract

Thermodynamical fluctuations impose random noise on the position of optical components. It is predicted that this thermal noise will limit the sensitivity of interferometric gravitational-wave detectors in their most sensitive frequency band. Thermal noise originating from optical coatings was first considered in the context of interferometric gravitational wave detectors. Its true significance was, however, only revealed after Y. Levin introduced a new method in 1998 to calculate the resulting phase noise of a laser beam reading out the position of a coated mirror. A result of this analysis is that the reflective optical coatings introduce a particularly large portion of thermal noise.

As a consequence, coating thermal noise is expected to prevent the detection of the standard quantum limit; a limitation to the sensitivity of an interferometric measurement caused by quantum fluctuations in the optical field. Elimination of the coating thermal noise will increase the likelihood of the successful observation of the standard quantum limit, thus enabling the investigation of quantum noise in the regime of optical squeezing. This project investigated a means to eliminate the effects of coating thermal noise, with the design and characterisation of a highly reflective coating-free mirror. This mirror utilised the phenomenon of total internal reflection and the Brewster angle to reflect light without the use of coatings. The dimensions of the mirror were governed by its expected implementation in an experiment to measure the standard quantum limit.

The design of the coating-free mirror undertaken as the initial part of this project is presented in detail. Once a CFM had been created according to this design, its spatial dimensions were measured. The weight of the mirror is 0.43 ± 0.01 g, well within the design goal of 0.5 g.

In order to analyse the reflectivity of the coating-free mirror it was incorporated, together with a high quality conventional mirror, into a triangular ring cavity. This cavity was stabilised to the laser frequency by the Pound-Drever-Hall technique. This enabled the interrogation of the stable cavity properties by an AM-sideband transfer scheme. The reflectivity of the mirror was analysed for optimum rotational alignment and as a function of its rotational alignment angle. The maximum reflectivity deviated from the expected value calculated from the mirror design. Most of the excess loss was attributed to scattering due to surface roughness at the points of total internal reflection and a necessary deviation from the Brewster angle due to the geometry of the cavity combined with the flat front face of the coating free mirror.

For optimum alignment a cavity finesse of about 4000 was measured, corresponding to a reflectivity of the coating free mirror of 99.89%. Thus, the objective of creating a highly reflective lightweight coating-free optic was achieved. The obtained reflectivity can be further increased by using a substrate that is super polished at the faces of total internal reflection.

Contents

Declaration	iii
Acknowledgements	v
Abstract	vii
Contents	ix
List of figures	xiii
List of tables	xv
Acronyms	xvii
1. Introduction	1
1.1. Gravitational Wave Detection	2
1.1.1. Noise in an Interferometric Gravitational-Wave Detector	3
1.2. Reaching the SQL	6
1.3. Coating Thermal Noise	8
1.3.1. Fluctuation-Dissipation Theorem	8
1.3.2. The Levin Method	8
1.3.3. Loss in the coating	9
1.4. Proposed Solutions	11
2. Control and Characterisation of a Two-Mirror Cavity	15
2.1. The Gaussian Beam	15
2.1.1. Beam Parameters	16
2.1.2. Hermite-Gaussian Beams	17
2.1.3. Intensity	18
2.2. The Fabry-Perot Resonator	19

2.2.1.	Cavity Loss	20
2.2.2.	Cavity Resonance	21
2.2.3.	Cavity Characterisation	22
2.3.	Cavity Stability and Mode Matching	23
2.4.	Polarisation	25
2.5.	Modulation and Cavity Control	26
2.5.1.	Modulation	26
2.5.2.	The Pound-Drever-Hall Locking Technique	28
2.5.3.	Cavity Interrogation with an Amplitude Modulated Beam	29
2.6.	Summary	30
3.	Mirror Design	31
3.1.	Electromagnetic Waves in matter	31
3.1.1.	Snell's Law and TIR	31
3.1.2.	The Fresnel Equations	32
3.1.3.	The Brewster Angle	33
3.2.	Coating-Free Mirror Concept	34
3.3.	Design for Experiment	35
3.3.1.	CFM Size	36
3.3.2.	Corner Angle	36
3.3.3.	CFM Reflectivity	39
3.3.4.	CFM Rotation	40
3.4.	CFM Cavity Equations	42
4.	Experimental Setup and Results	45
4.1.	Experimental Layout	45
4.2.	Measured Mirror Geometry	47
4.3.	Modematching	48
4.4.	Cavity Alignment	50
4.5.	Cavity Scan	51
4.5.1.	FWHM and FSR	52
4.5.2.	Beam Transverse Alignment	53
4.6.	Control System	54

4.6.1. Servo and PZT Frequency Response	54
4.6.2. Locking the Cavity	55
4.7. CFM Reflectivity	56
4.7.1. AM-Sideband Cavity Interrogation	56
4.7.2. CFM Reflectivity	57
4.7.3. CFM Rotation Calibration	58
4.7.4. Reflectivity Vs. Rotation	58
4.7.5. Non-Perfect Total Internal Reflection	59
4.8. Intracavity Power	60
4.9. Transverse Electric Polarisation	61
4.10. Summary	62
5. Summary and Future Work	63
5.1. Summary	63
5.2. Future Work	64
A. ABCD Matrices	67
B. Tabulated Experimental Data	69
C. The Relationship Between Finesse, FWHM, and FSR	71
Bibliography	75

List of figures

1.1. Sensitivity of Advanced LIGO	5
1.2. Shot Noise and Radiation Pressure Noise	6
1.3. Braginsky's design for corner reflectors	11
1.4. Giazotto's design for corner reflectors	12
1.5. Khalili's desing to reduce coating thermal noise	12
2.1. Gaussian beam parameters	18
2.2. 3D profile of TEM ₀₀	19
2.3. A Fabry-Perot resonator	19
2.4. Phasor diagram of optical resonator with different detunings	22
2.5. Amplitude and phase response of Fabry-Perot cavity	23
2.6. Three different polarsations	26
2.7. The polarisation vector after passing through an amplitude modulator and quarter-wave plate	28
2.8. Cosine and sine amplitude and phase modulation	29
2.9. The reflected intensity and error signal for a 50 cm cavity	30
3.1. Perspective drawing of the CFM	31
3.2. A beam incident on a dielectric interface	32
3.3. Transmitted and reflected power at a dielectric interface for TM polarised light	33
3.4. Transmitted and reflected power at a dielectric interface for TE polarised light	34
3.5. The coating free mirror concept	35
3.6. Information pertaining to CFM dimesions	37
3.7. Trajectory of light incident on the corner	37
3.8. The cavity length as a function of the change in corner angle δ	38
3.9. The dimensions of the CFM design for this experiment	39
3.10. Beam trajectories as the CFM is rotated	41
3.11. The reflectivity as a function of CFM rotation	41

4.1. Experimental layout	46
4.2. Measurement of the CFM angles	47
4.3. The CFM dimensions, as measured in this experiment	48
4.4. The calculated beam width and radius of curvature	49
4.5. The beam profile for the horizontal component of the beam	49
4.6. The rotatable stand used to hold the CFM	50
4.7. Misalignment of the CFM cavity	51
4.8. FWHM and FSR of the CFM cavity	53
4.9. Response of the Michelson interferometer used to obtain the PZT frequency response	55
4.10. Open loop frequency response of the PZT and the servo	55
4.11. Error signal of CFM cavity	56
4.12. The measured frequency response of the CFM cavity	57
4.13. Reflectivity of the coating-free mirror as a function of rotation	59
4.14. Photographs of CFM with cavity on resonance	60
4.15. The effect of mirror rotation on the position where the beams converge	60
4.16. The power reflected from the front face of the CFM as a function of rotation	61
4.17. A close-up scan of the frequency response of the cavity for the TE polarisation	62
5.1. A design of an all coating free dual-recycled Michelson interferometer	65
A.1. Optical components (left) and their corresponding ABCD matrices (right)	67
C.1. A triangle as used in order to re-express the arccos expression for ϕ in terms of arctan	72
C.2. Approximation and exact representation of cavity finesse	74

List of tables

B.1. The finesse of the cavity as calculated for each measured reflectivity . . .	69
---	----

Acronyms

AM	Amplitude modulation
AdvLIGO	Advanced LIGO
CFM	Coating free mirror
CTE	Coefficient of thermal expansion
CTD	Coefficient of thermal diffusion
EOM	Electro-optic modulator
IGWD	Interferometric gravitational-wave detector
FSR	Free spectral range
FWHM	Full width at half maximum
LCGT	Large Cryogenic Gravitational-wave Telescope
LIGO	Laser Interferometer Gravitational-wave Observatory
PD	Photo detector
PM	Phase modulation
ppm	Parts per million
SQL	Standard quantum limit
TIR	Total internal reflection

Chapter 1.

Introduction

With the increasing sensitivity of high precision interferometric experiments such as gravitational-wave detection, and endeavours to reach the standard quantum limit of interferometry (SQL), the quality of optical coatings has become more relevant. The optical quality of the mirror coatings has dramatically increased in recent years, however, the aspect of the mechanical properties of optical coatings has long been neglected. While the mechanical properties are of no significance for standard applications, they are of crucial importance for interferometric gravitational-wave detectors (IGWDs), as well as for experiments aiming to reach the SQL. However, it was not until a novel method of calculating the thermally driven displacement noise associated with optical coatings was proposed by Yu. Levin [Levin '98] in 1998, that the significance of coating thermal noise was revealed.

The so called normal-mode decomposition approach was commonly used to derive the thermal noise associated with the test masses. Although it gave excellent results for the thermal noise of bare test mass substrates, this approach fails to take inhomogeneously distributed loss appropriately into account. Consider, for example, the 40 kg test masses of Advanced LIGO, which have a coating layer of a few microns in thickness. The mechanical quality factor of the test mass substrate comprised of high quality fused silica is much higher than that of the optical coating, and as such, in a coated test mass, the loss is extremely inhomogeneously distributed. Since the coating is in direct interaction with the laser beam that reads out the test mass position, the thermal noise of the coating is of far greater importance than the normal mode decomposition method would suggest. As a consequence, the introduction of the Levin method revealed that the contribution to the thermal displacement noise by the optical coatings was greater than previously expected, and is the dominant source of thermal noise associated with the test masses ¹. In fact, coating thermal noise is expected to limit the sensitivity of Advanced LIGO in its most sensitive frequency band.

The significance of coating thermal noise was discovered in the wake of the quest to build IGWDs, however, it is an even more severe problem for experiments aiming to reach the SQL. In fact, according to the calculations undertaken so far, it is unclear whether the SQL can be reached at all with the currently available coatings. The challenges with such experiments result from the fact that short Fabry-Perot cavities must be employed, in order to enable the observation of small length fluctuations, and to reduce the sensitivity

¹As an interesting side effect the influence of the attachment of small magnets to the rear sides of the test masses, as is done in LIGO for the feedback actuators, was initially estimated to be a factor of 15 greater than that predicted using Levin method [Yamamoto '01]

of the setup to fluctuations of the laser frequency. From the theory of optical resonators, presented in Chapter 2, it is evident that the laser spot size in a short cavity needs to be small to fulfil the stability criterion. As we will see in the following sections, the thermal noise of mirrors and their coatings scales inversely with the diameter of the interrogating laser beam, which can be understood as averaging the displacement noise at the surface of the mirror over the area of the incident beam.

When designing an SQL experiment, the coating noise can be circumvented with the implementation of a mirror with no optical coating. Such a mirror is required to be used as an opto-mechanical coupler, such that it efficiently couples quantum fluctuations in the light field to displacement. Maximum displacement will occur in this regime when the inertia of the sensor is minimised. Thus, it is desirable to minimise the mass of the coating free mirror, limited by the necessity to limit diffraction loss of the laser beam. Hence, the mass of the mirror was restricted to be no greater than 0.5 g. The design and characterisation of such a mirror with no optical coating was the objective for the work described in this thesis.

The structure of this thesis is detailed as follows:

Chapter 1 motivates the project by placing it in the context of experiments in which coating thermal noise is expected to be a limiting factor. Following this, the mechanisms that give rise to coating thermal noise are discussed. The chapter ends with an examination of the previously proposed solutions to the problem of coating thermal noise.

Chapter 2 introduces the relevant theory of optical resonators and an introduction to cavity control.

Chapter 3 describes the design of the coating-free mirror, its expected limitations, and its capacity to reflect light under rotational misalignment. In order to characterise the coating-free mirror it is incorporated into an optical cavity. The equations describing this cavity are presented.

Chapter 4 provides a detailed account of the processes undertaken in setting up the experiment in conjunction with the experimental results. This includes a full characterisation of the mirror in terms of its dimensions, reflectivity, and limitations.

Chapter 5 starts with a summary of the project outcome and considers in what way the experiment could be improved. Some interesting ideas for further work involving coating free optics concludes the thesis.

1.1. Gravitational Wave Detection

In 1916, Albert Einstein revolutionised gravitational theory with the publication of his general theory of relativity. He describes a universe in which mass was intrinsically linked with the curvature of spacetime - the 4-dimensions of space and time - and that this curvature accounted for what is observed as the force of gravity. Instantaneous

gravitational action at a distance - a consequence of Newton's gravitational theory - was also accounted for by the new formalism, which postulated that a disturbance in the fabric of spacetime travels at the speed of light. A consequence of Einstein's theory of general relativity is that a change in quadrupole momentum of a given mass distribution results in the emission of gravitational waves. Although these gravitational waves carry a large amount of energy, the coupling to objects through which they pass is incredibly small. This means that a gravitational wave will contain information that has been largely unaffected during its journey.

While the early universe was opaque for electromagnetic radiation until about 380,000 years after the big bang, gravitational waves were not subject to this restriction. Thus, it is expected that gravitational waves contain information about the universe from as early as 10^{-43} s after the big bang. Information about the universe at this early stage is unable to be directly detected by any other means.

The weak coupling of gravitational waves to matter also means, however, that gravitational waves are hard to detect. A gravitational wave is predicted by the existing theoretical models to impart a strain of not more than $h \leq 10^{-21} / \sqrt{\text{Hz}}$ on a ground based gravitational wave detector.

The most promising approach to detect gravitational waves on earth is based on Michelson interferometers. These IGWDs have an inherently broad band response to gravitational waves, spanning a frequency band from about 50 Hz to a few kilohertz. Due to the quadrupole nature of gravitational waves, a Michelson interferometer is an ideal device for their detection. A gravitational wave propagating orthogonal to the plane of the interferometer alters the path length in the arms in a differential manner, and thus couples some of the light power within the interferometer to the output port.

1.1.1. Noise in an Interferometric Gravitational-Wave Detector

The chief goal during the commissioning of a IGWD is the reduction of noise that may couple to the interferometer output port. This will increase the signal to noise ratio of a gravitational wave signal, increasing the confidence with which claims of a successful detection can be made.

Seismic Noise

The test masses in an IGWD need to be isolated from seismic disturbances by many orders of magnitude (i.e. about ten orders of magnitude at 100 Hz). In order to obtain this isolation they are suspended from pendulums, which act as a low pass filter for seismic vibrations. A simple pendulum has a response to a driving force that scales as $1/f^2$ above its resonance frequency. The suspension systems of the IGWDs are designed to have a low resonance frequency so that the suspended test masses are well isolated in the band of interest. Further isolation can be obtained by cascading pendulums, which provides attenuation that scales as $1/f^{2n}$, where n is the number of suspension stages; GEO 600, for example, uses triple cascaded pendulums for their isolation systems [Plissi '00].

Thermal Noise

In the current generation of the gravitational wave detectors, thermal fluctuations of the interferometer test masses or their suspensions will predominate over quantum noise in the most sensitive frequency band. Random thermal fluctuations in the test masses and their suspensions provide uncorrelated changes in the path lengths of the two beams within the interferometer. The fluctuation-dissipation theorem (see Section 1.3.1) relates this thermal noise directly to the material's mechanical quality factors Q , where the Q is inversely proportional to the loss in the material. Loss can arise from anelasticities in the material (bulk loss), from the thermoelastic effect due to a nonzero coefficient of thermal expansion, or from the nonlinear thermoelastic effect due to the thermal dependence of the Young's modulus. Much research has been conducted regarding these loss mechanisms. For detailed descriptions see e.g. [Gillespie '94, Gillespie '93, Willems '99, Willems'02, Kajima '99, Cagnoli '02].

As a result of the scaling of thermal noise with the loss in the material, it is desirable to have a test mass that is both of high optical and high mechanical quality. Current and future IGWDs plan to use either fused silica (AdvLIGO) or sapphire (LCGT) for their test mass substrate material. Also, cooling of the interferometer test masses is planned for Japan's LCGT, the proposed Large Cryogenic Gravitational-wave Telescope, in order to reduce thermal noise. In the absence of cooling, the greatest contribution to thermally induced displacement noise of the test mass surfaces is due to Brownian thermal noise in the optical coatings. This is explained by internal friction of the combined coating materials, introducing excess loss. As the detrimental effects of coating thermal noise were the main motivation for this project, a detailed exploration of this topic is undertaken in Section 1.3.

Due to suspension systems and test masses of higher quality, the thermal noise of these components can be lowered by about one order of magnitude for the next generation of IGWDs. However, thermal noise of the optical coatings is still expected to be the limiting noise source in the most sensitive frequency band of AdvLIGO. Figure 1.1 shows the predicted sensitivity curve of AdvLIGO. This sensitivity plot was generated using the matlab program *BENCH*².

Quantum Noise

The frequency of the laser is stabilised to a reference cavity in the interferometer. This can be done by using, for example, the arm cavities of the LIGO interferometer, as they provide an excellent frequency reference above the resonance frequency of the pendulum suspensions. The power of the laser is stabilised by means of a noise eater, where a small amount of the laser beam is tapped off and sent to a photodetector. Any change in power is detected and the according control signal is sent back to the laser. However, there is a limit to which the laser power and frequency can be stabilised. The Heisenberg uncertainty principle (HUP) places a lower bound on the product of the uncertainties of the two non-commuting variables of amplitude and phase, and this uncertainty manifests itself as quantum noise.

²Thanks to Greg Harry from the LIGO group at MIT for supplying this program

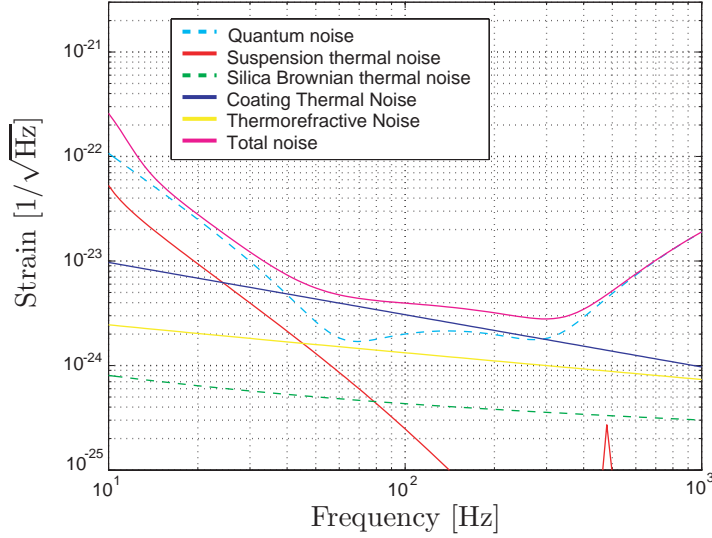


Figure 1.1.: The calculated amplitude spectral density of the noise expected for Advanced LIGO. This detector is limited by radiation pressure noise at low frequencies, shot noise at high frequencies, and thermal noise from the optical coatings in the most sensitive frequency band.

In an IGWD, a phase uncertainty limits the extent to which the interference of the two beams can be measured. This is known as shot noise. Shot noise is white noise; it is constant for all frequencies, and it scales inversely with the square root of the laser power. Hence, the signal to noise ratio (SNR), for shot noise increases with the optical power,

$$\text{SNR}_{SN} \propto \sqrt{P} \quad (1.1)$$

where P is the power of the optical field in the interferometer. Shot noise is reduced in an IGWD with the addition of a *power recycling mirror*. As the interferometer is locked to the dark fringe operation condition, all light is reflected back to the input port (symmetric port). By placing a mirror, the power-recycling mirror, at this port the light is re-injected into the interferometer. This technique leads to a resonant enhancement of the light power inside the interferometer, thus reducing the shot noise.

The quantum amplitude uncertainty between the two beams in a Michelson can be considered as a random fluctuation in the photon number. Phase and amplitude fluctuations are caused by quantum vacuum fluctuations entering the interferometer through the output, or anti-symmetric, port [Caves 80]. Hence, the photon number fluctuation is anti-correlated for the respective arms. As the relative number of photons in each arm fluctuates, the momentum transferred to the end mirrors is different, and the michelson differential mode is stimulated at random, introducing noise to the output port. The momentum transfer is governed by the response of the end mirrors, and as such, radiation

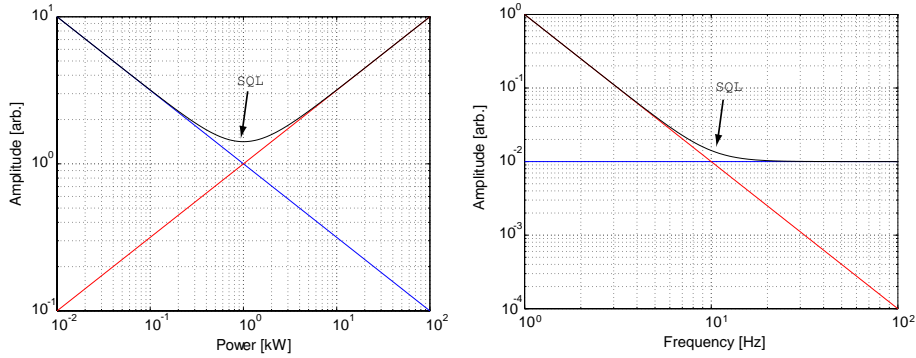


Figure 1.2.: Shot noise (blue) and radiation pressure noise (red) as a function of power for a given frequency (left), and as a function of frequency for a given power (right).

pressure noise (RPN) is proportional to this response. RPN decreases with the inverse square root of the light power, and accordingly

$$\text{SNR}_{RPN} \propto \frac{1}{\sqrt{P}} \quad (1.2)$$

Radiation pressure noise and shot noise at a given frequency scale inversely with respect to each other, as a function of laser power, so there is a power at which these two are equal in magnitude. Conversely, as a function of frequency, there is an according point at which the two noises are equivalent for a given power. This is known as the standard quantum limit (SQL), and in the absence of squeezing, it corresponds to the optimum sensitivity that can be achieved for an interferometric measurement. A successful experiment to measure the SQL would provide the first experimental observation of the entire quantum noise spectrum of an opto-mechanical system. Furthermore, it would allow investigations of the spectral response of this system in the presence of squeezed light, which promises to increase the sensitivity of future gravitational-wave detectors [McKenzie '02, Vahlbruch '05, McKenzie 06, Vahlbruch '06].

Figure 1.2 shown SN and RPN as a function of power, and as a function of frequency.

1.2. Reaching the SQL

In Section 1.1.1 the importance of quantum noise in the field of gravitational wave detection was pointed out. This motivates the implementation of an optomechanical system in which the SQL is observable. Such a setup is not only of fundamental interest, as experimental observations are always desired in order to validate theoretical predictions, but will also allow the investigation of feasible optical squeezing regimes for future detectors. In order to arrange an experiment to measure the SQL, an opto-mechanical sensor that is sensitive to quantum phase and amplitude fluctuations in the optical field must be implemented. The detection of shot noise, or quantum fluctuations in the phase of the light, requires that the opto-mechanical sensor enact interference of the beam by the use of an interferometer or a test cavity. The opto-mechanical coupler transfers quantum

fluctuations in the amplitude of the light field to displacement fluctuations and can be built using a pendulum suspension or a torsion balance. The setup needs to be isolated from seismic vibrations, the classical properties of the optical field stabilised, and the optics and their suspensions are required to have a high enough mechanical quality, in order that thermal fluctuations do not predominate.

The dimensions of this interferometer are required to be small in order to make the setup sensitive for small length changes introduced by radiation pressure noise. As the system will be locked using the Pound-Drever-Hall method, length fluctuations are equivalent to laser frequency fluctuations. Hence, the cavity length fluctuations can be read out at the error point of the stabilisation loop. The cavity strain, as it corresponds to the change in laser frequency, is illustrated by the following equation

$$\frac{\Delta\nu}{\nu} = \frac{\Delta L}{L} \quad (1.3)$$

where ν is the frequency of the laser, and L is the cavity length. Additionally, for a small cavity, the stability criterion requires that the beam size be small.

The optics of the interferometer or test cavity must be suspended such that they are sensitive enough to react sufficiently to displacements due to radiation pressure. Radiation pressure displacements can be increased by raising the laser power. This, however, comes at the expense of observable shot noise. Thus, it is preferable to minimise the mass, or moment of inertia, of the suspended optics, in order to reduce the optical power required for detection of radiation pressure noise. Care must be taken that reduction in the dimensions of the optic are not too great such as to cause diffraction loss in the incident beam. A small beam size is desirable for this reason also.

At this point, thermal noise in the optics becomes an important consideration. This can be minimised with the choice of a constituent material of a high mechanical quality. Conventional optics employ coatings in order to reflect light, which causes a considerable reduction in the mechanical quality of the system with which the beam interacts. As is shown in Section 1.3, this is furthered by the fact that the thermal displacement noise, resulting from direct interaction with the optical coatings by the laser beam, is considerably higher for a small beam size. Hence, the design and implementation of a reflector with no coatings promises to allow the use of a small beam, with a decreased risk that thermal fluctuations override the quantum effects in this regime. This provides the means to lower the moment of inertia of the system, with a decrease in the power required for the observation of radiation pressure noise. An according rise in relative shot noise increases the likelihood of measurement of the standard quantum limit.

Once the SQL has been reached, the experimental setup can be used to investigate the possibility of achieving sub-SQL sensitivity by the use of squeezed states of light. This can be done by the injection of a squeezed vacuum into the interferometer via the antisymmetric port. To increase the whole sensitivity curve, the rotation angle of the squeezing ellipse has to be adjusted accordingly; amplitude squeezing has to be used where radiation pressure noise dominates while phase squeezing has to be used where shot noise dominates. Such a frequency dependent variation of the squeezing ellipse was demonstrated by S. Chelkowski et al. [Chelkowski'05]. The achievable sensitivity of such a setup is

theoretically only limited by the available squeezing strength, provided that there is no other limiting noise in the system.

There are currently four experiments being planned to reach the SQL; One at the Max-Planck Institute for Gravitational Physics in Hanover, Germany, one at the MIT, one in Tokyo, and one at the Centre for Gravitational Physics at the ANU [Goßler]. The experiment at the ANU will be based on a torsion balance as the opto-mechanical sensor. This torsion balance will be made from a fused silica bar, suspended from a thin fused silica fibre. The torsion bar will support both end mirrors of an arm cavity Michelson interferometer. In order to have a low inertia, the weight of the torsion bar must not exceed 1.5 g. Hence, the limitation on the weight of the mirrors to be not more than 0.5 g each. This experiment provides the main motivation for the work of this thesis.

1.3. Coating Thermal Noise

The motivation to eliminate optical coatings has been provided in the preceding sections. Here, a detailed discussion of thermal fluctuations in a reflective optic due to dielectric optical coatings is presented. These fluctuations result from physical processes that are described by the Fluctuation-Dissipation Theorem (FDT).

1.3.1. Fluctuation-Dissipation Theorem

The fluctuation-dissipation theorem was first presented by Callen and Welton in 1951 [Callen '51, Callen '52]. It asserts that a linear dissipative system in thermal equilibrium experiences random thermal fluctuations, and that there is an intrinsic relationship between the amount of dissipation in the system and the magnitude of these fluctuations. For example, a resonator with a relatively high loss will exhibit a large degree of thermally induced fluctuations. Conversely, for resonators with a low loss, or high mechanical quality factor Q , the thermal noise is minimised.

1.3.2. The Levin Method

Until the introduction of the Levin method, calculations of the thermally driven displacement noise of a test mass were done via normal mode decomposition. This method involves summing over a large number of internal modes, and can be computationally expensive; especially for a small laser beam, where this sum converges very slowly. A much more severe drawback of the normal mode decomposition method lies in the fact that it is only valid when the sources of loss are homogeneously distributed over the test mass volume. For a test mass with inhomogeneously distributed loss, the normal mode approach breaks down. As pointed out in the introduction of this chapter, the loss in a AdvLIGO test mass are extremely inhomogeneously distributed: The test mass substrate weighs 40 kg and is made from high quality fused silica, which has a mechanical quality factor of about $Q_{\text{substrate}} \simeq 10^8$. The coating, however, is only of a thickness of a few microns and has a mechanical quality factor of the order $Q_{\text{coating}} \simeq 10^4$.

The method introduced in 1998 by Levin uses a direct application of the fluctuation-dissipation theorem to derive an analytic expression for the problem. The obtained ex-

pression reflects the resulting fluctuations in the phase of the sensing laser beam. The approach is based on applying an oscillatory pressure $P(\vec{r}, t) = F_0 \cos(\omega t) f(\vec{r})$ to the surface of the mirror. The spatial distribution $f(\vec{r})$ of the pressure is the same as that of the Gaussian profile of the interrogating laser beam. For obvious reasons the Levin method is also referred to as the Levin pressure approach. Its most significant implication for this project is the fact that it shows that the thermal noise due to loss located near the mirror surface, as sensed by the laser beam, scales with the beam radius w_0 as $1/w_0^2$. Since the normal mode decomposition does not take the location of the loss into account, this result differs from previous predictions; by a factor of $1/w_0$. As required, the two methods converge under consideration of the thermal noise due to loss inside the substrate, which scales with the laser beam radius as $1/w_0$.

The strong scaling of coating thermal noise with the laser beam radius is obviously of severe consequence when working with small beam radii. As described in Section 1.2, this is the case for experiments aiming to reach the standard quantum limit.

1.3.3. Loss in the coating

With the increasing sensitivity of the proposed interferometric gravitational-wave detectors, the demands on the thermal noise performance related to the test masses are increasing accordingly. The Levin method allows accurate calculations of the thermal noise of a coated test mass if input parameters such as the dimensions and mechanical quality factors of the substrate and the coating, as well as the parameters of the interrogating laser beam, are known to the according precision. These quantities have to be obtained or inferred from measurements undertaken beforehand.

At this point in time, the mechanisms by which this loss occurs are unknown, and ongoing experiments continue to probe the properties of the coating, in order to gain a better understand of this [Harry '02, Braginsky '03, Crooks '04]. These involve varying the number of coating layers, the individual layer thickness, and the materials from which the coatings are comprised. The coating is formed from alternating layers of two materials, one of which is the substrate material, that are ion sputtered onto the surface of the substrate. Silica (SiO_2) is of a sufficient optical and mechanical property to form the low refractive index constituent of the coating. However, the high refractive-index constituent is a subject of ongoing investigations. The candidate materials to form the high refractive-index constituent are tantala (Ta_2O_5) or alternatively alumina (Al_2O_3), which has a lower internal loss [Crooks '04]. Regarding the mechanical quality of the coating materials, two contributions to the displacement noise must be taken into account: the displacement noise due to dissipation by anelasticities, otherwise known as internal friction, and thermoelastic noise.

Internal friction

It can be shown that for a coating of thickness l the power spectral density of the thermally driven displacement noise due to anelasticities of a coated mirror is of the form [Rowan '05,

Harry '02]

$$\hat{X}_{\text{mirror}} \simeq \frac{4k_B T}{\sqrt{2\pi}\omega} \frac{1 - \sigma^2}{E w} \cdot \left(\phi_{\text{substrate}} + \frac{2}{\sqrt{\pi}} \frac{1 - 2\sigma}{1 - \sigma} \frac{l}{w} \phi_{\text{coating}} \right) \quad (1.4)$$

Here k_B is the Boltzmann constant, T is the temperature, E is the Young's modulus, w is the beam radius, σ is the Poisson's ratio, and ϕ is the loss. This is a simplified approach, derived for a semi-infinite test mass, under the assumptions that the Young's moduli and Poisson's ratios of the coating are similar in the directions parallel and perpendicular to the coating. Although, in general, this is not the case, this is a reasonable assumption for a coating comprised of alternating layers of SiO_2 and Ta_2O_5 , as the values for these materials are similar. Consequently, they can be assumed to be of the same value as those of the mirror substrate in the case of a fused silica mirror³ Lastly, it is assumed that the internal friction occurs in the coating materials themselves and is not due to friction between the coating layers, in which case the number of coating layers, rather than the thickness of the coating, had to be accounted for. [Harry '02]

All parameters in the above equation can be taken from the literature values except for the loss of the substrate and the coating. Values for these quantities have to be obtained by ring-down time measurements. The loss of a LIGO size (25 cm diameter, 10 cm thickness) fused silica substrate was measured by P. Willems at Caltech to be smaller than $\phi < 10^{-8}$. The loss of multilayer optical coatings of the above described materials was measured by [Crooks '04] to be in excess of $\phi > 1.5 \cdot 10^{-4}$, which if of the same order as those measured by [Harry '02]. A direct measurement of coating thermal noise has been performed by E. Black in the thermal noise interferometer at Caltech [Black '04]. The results were found in good agreement with Equation 1.4. K. Numata performed another direct measurement of coating thermal noise [Numata '03] that agreed well with the coating thermal noise of a half-infinite test mass, derived from an method equivalent to the Levin method [Nakagawa '02] used in the derivation of Equation 1.4.

Thermoelastic loss

Although the loss related to internal friction dominates the thermal noise of a coated mirror, the contribution due to thermo-elastic loss should to be taken into account for a full analysis. A simplified approach to obtain the power spectral density due to thermo-elastic loss in a multilayer coating of thickness l , made of two materials labelled a and b of thickness d_a and d_b , respectively, yields

$$\hat{X}_{\text{coating}}^{\text{thermo elastic}} = \frac{8\sqrt{2}k_B T^2}{\pi\sqrt{\omega}} \frac{l^2}{2w^2} (1 + \sigma_s)^2 \frac{C_{\text{avg}}^2}{C_s^2} \frac{\alpha_s^2}{\sqrt{D_s C_s}} \Delta^2 \quad (1.5)$$

³For sapphire, another material proposed for future detectors, this approximation can not be used, due to the higher Young's modulus. The mismatch in Young's modulus of the substrate and the coating is likely to lead to a higher contribution of coating thermal noise due to loss in the plane perpendicular to the coating.

where C is the heat capacity, α is the coefficient of thermal expansion (CTE), and D is the coefficient of thermal diffusion (CTD). Subscript s refers to a substrate property and

$$\Delta^2 = \left\{ \frac{C_s}{2\alpha_s C_{\text{avg}}} \left(\frac{\alpha}{1-\sigma} \left[\frac{1+\sigma}{1+\sigma_s} + (1-2\sigma_s) \frac{E}{E_s} \right] \right)_{\text{avg}} - 1 \right\}^2 \quad (1.6)$$

To carry out the averaging an operator of the form

$$(X)_{\text{avg}} = \frac{d_a}{d_a + d_b} X_a + \frac{d_b}{d_a + d_b} X_b \quad (1.7)$$

is used [Rowan '05, Fejer '03]. In order to reduce the thermoelastic noise, it would be desirable to have a common coefficient of thermal expansion of the mirror material and the coating materials.

1.4. Proposed Solutions

Some different designs for mirrors without reflective coatings have previously been proposed.

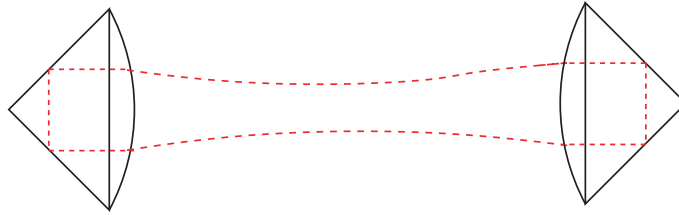


Figure 1.3.: Braginsky's design includes a lens at the front of the mirror in order to focus the beam. It also incorporates an anti-reflective coating to allow efficient in and out-coupling of the light to the prism.

In 2004, V. B. Braginsky and S. P. Vyatchanin [Braginsky '04] presented a design for a fused silica prism that reflects light from a corner reflector, using total internal reflection. Stability of a cavity comprised of these mirrors was accounted for with the addition of a convex curved surface at the input of the mirror. Light was prevented from being promptly reflected from the front face by adding an anti-reflective coating to this surface. The Gaussian beam is collimated by this front face before it is incident on the reflecting corner. The centre of the beam, corresponding to the point of maximum intensity in the transverse direction, is incident at the corner, and the discontinuity in the prism shape here causes some of the incident light to be lost. Also, the anti-reflective coating causes a certain amount of coating thermal noise. Even though the coating thermal noise will be much lower than that of a highly reflective coating it may still be too high for conducting measurements with sub-SQL sensitivity.

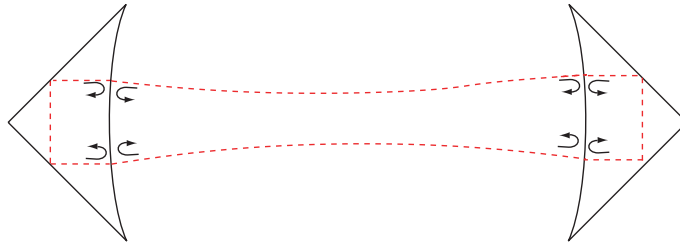


Figure 1.4.: Giazotto's design matches the front of the reflector to the radius of curvature of the beam. The rear reflectors are slightly curved to maintain cavity stability. Problems arise with the requirement that the light exiting the prism have a defined phase relationship with the promptly reflected light.

At the Italy-Australia Workshop on Gravitational Waves in October, 2005, A. Giazotto and G. Cella presented a similar design using total internal reflection [Giazotto '05]. The front surface of this mirror is concave, such that it matches the radius of curvature of the incident beam. Without an anti-reflective coating, part of the incident beam is reflected from the front face of the prism. The fraction transmitted into the prism is reflected by the corner back towards to curved surface. Once it passes through this surface, its width and radius of curvature are equivalent to that of the promptly reflected beam, and their relative phase gives rise to interference. Thus, this design in fact describes an interferometer, with unwanted phase matching considerations that must be accounted for. It is desired that the two beams reflected from the mirror interfere constructively. This places strict requirement on the prism properties; spatial dimensions, thermal expansion, and refractive index homogeneity must all be extremely well characterised for the mirror for optimum reflection. Additionally, the light leaving the prism will accordingly partially reflect from the concave front surface. This small fraction of the light is scattered out of the stable cavity mode.

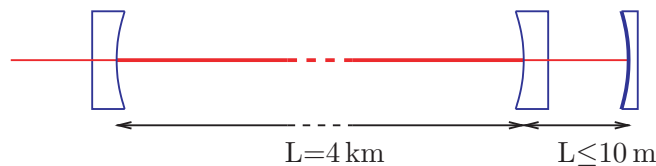


Figure 1.5.: Khalili's design uses a short Fabry-Perot cavity, depicted here at the end of a LIGO arm. The thickly coated mirror is contained within the cavity, and thermal noise associated with this coating is suppressed by as much as 10^3 . This design comes at the expense of an extra length degree of freedom that must be controlled.

F. Khalili [Khalili '04] proposed to use a Fabry-Perot cavity at the end of the interferometer arms, in the place of the end mirror. This Fabry-Perot is to be held on anti-resonance such that it is highly reflective. The first mirror of the cavity is a mirror of moderate reflectivity, i.e. less coating layers, while the second mirror is a highly reflective mirror with a coating layer of normal thickness. The anti-resonant cavity rejects most of the light in-

cident on it, and there is an according reduction in the amount of the light that interacts with the normally coated mirror. This design promises to reduce thermal noise introduced by the coating of the highly reflective mirror by a factor of 10^3 , and the reflectivity of the cavity in this regime promises to be an order of magnitude higher. The coating noise in the moderately reflective optics - the arm cavity mirror and the first mirror in the Fabry-Perot - are not suppressed, but are much lower than that usually provided by the highly reflective mirror. This design suppresses the coating thermal noise in the interferometer substantially, and has promising applications to the reduction of coating thermal noise in a gravitational wave detector, and for an experiment to measure the SQL, despite the added complexity of the arrangement. It remains desirable, however, to avoid coating thermal noise altogether, as it is unknown how far below the SQL future squeezing experiments may venture.

Chapter 2.

Control and Characterisation of a Two-Mirror Cavity

This project consisted of the design and characterisation of a highly reflective coating-free mirror (CFM). The characterisation of the CFM was performed by including it as a cavity mirror in a two-mirror cavity. The cavity properties were then examined in order to infer information about the CFM. An overview of the theory required for the experiment is presented in this chapter. Initially, a discussion of the general properties of a laser beam is presented, as a basis for the setup of a Fabry-Perot resonator. A detailed introduction to the Fabry-Perot resonator is provided. This included a presentation of the cavity equations, cavity parameters, theory regarding the fundamental cavity eigenmode, and mode-matching the input beam to it.

Next, the theory of an active control system, used to maintain cavity resonance, is presented. We used the Pound-Drever-Hall locking technique [Black '00] for this purpose. A description of amplitude and phase modulation is presented, and finally, a technique to interrogate the cavity frequency response, using an amplitude modulation transfer function, is described.

The properties of the stabilised cavity can then be interrogated by amplitude modulated sidebands, and description of how this is achieved completes the chapter. This technique provides an indirect yet accurate means to determine the reflectivity of the CFM.

2.1. The Gaussian Beam

The laser beam is a paraxial wave, defined as a plane wave modulated by an envelope which is a slowly varying function of position, or approximately constant over the distance λ . This is the *slowly varying envelope approximation* (SVEA). The spatial properties of such a wave are described by its complex amplitude,

$$U(\mathbf{r}) = A(\mathbf{r}) \exp(-ikz) \tag{2.1}$$

represents a plane wave, $\exp(-ikz)$, modulated by the slowly varying complex envelope $A(\mathbf{r})$, $k = 2\pi/\lambda$ is the wavenumber, and λ is the wavelength of the light. The complex amplitude of a paraxial wave is determined by substitution of $A(\mathbf{r})$ into the paraxial Helmholtz equation [Saleh, Teich '91],

$$\left(\frac{\partial^2}{\partial x^2} + \frac{\partial^2}{\partial y^2} \right) A(\mathbf{r}) - i2k \frac{\partial A(\mathbf{r})}{\partial z} = 0 \tag{2.2}$$

One solution to Equation 2.2 is the complex envelope of the Gaussian beam. Substitution into Equation 2.1 provides an expression for the complex amplitude of the Gaussian beam,

$$U(\mathbf{r}) = A_0 \frac{w_0}{w(z)} \exp \left[\left(-\frac{x^2 + y^2}{w^2(z)} \right) - i \left(kz - k \frac{x^2 + y^2}{2R(z)} + \xi(z) \right) \right] \quad (2.3)$$

This expression completely describes its spatial properties in Cartesian co-ordinates. The beam described by this equation has azimuthal symmetry around the z axis, with the amplitude maximum at $x = y = 0$. Equation 2.3 is arranged such that the wavefront radius of curvature $R(z)$, the beam radius $w(z)$, the waist size w_0 and the Guoy phase $\xi(z)$ are explicitly shown. These beam parameters can be expressed as follows,

$$w^2(z) = w_0^2 \left[1 + \left(\frac{z}{z_0} \right)^2 \right] \quad (2.4)$$

$$w_0^2 = \left(\frac{\lambda z_0}{\pi} \right) \quad (2.5)$$

$$R(z) = z \left[1 + \left(\frac{z_0}{z} \right)^2 \right] \quad (2.6)$$

$$\xi(z) = \arctan \left(\frac{z}{z_0} \right) \quad (2.7)$$

where z_0 is the Rayleigh length,

$$z_0 = \frac{\pi w_0^2}{\lambda} \quad (2.8)$$

2.1.1. Beam Parameters

Following the derivation of the Gaussian solution to the paraxial Helmholtz equation, a discussion regarding the beam parameters introduced above will help to elucidate these experimentally useful variables.

Beam Radius ($w(z)$)

The beam radius $w(z)$ is a measure of the width of the beam. It is defined as the transverse distance between the beam propagation axis and the point at which the real part of the beam amplitude is $1/e$ times the real axial amplitude. The beam radius necessarily changes with the propagation distance z , and a local minimum of $w(z)$ is known as the waist of the laser beam. Figure 2.1 displays the behaviour of the beam radius about the beam waist.

Waist Size (w_0)

A focused Gaussian beam does not converge to a point, as ray optics arguments suggest. The minimum size of the focused beam is known as the waist size, and increases with

increasing wavelength of light, and decreases with increasing convergence angle. Often, it is desirable to tailor the size of the waist to, for example, pass the beam through the aperture of an opto-electronic device such as an electro-optic modulator¹. This is usually done by focusing the beam with a lens of an appropriate focal length in order to alter the beam convergence/divergence angle.

Radius of Curvature ($R(z)$)

The curvature of the wavefront is generally expressed as the radius of a circle with the same curvature, and is denoted the radius of curvature $R(z)$. At the position of the beam waist, the radius of curvature is infinite, or that of a planar wave, and at distances far from the waist of the beam it varies linearly with z , mimicking the behaviour of a spherical wave. Knowledge of the radius of curvature is important in establishing self reproducing beams within optical resonators. Figure 2.1 displays the radius of curvature of the beam as a function of propagation distance, about the beam waist.

Guoy Phase ($\xi(z)$)

The $\xi(z)$ term in the exponential argument of Equation 2.3 represents a phase retardation at the beam axis as a function of propagation distance z . This is known as the Guoy phase. It is the difference in phase of the Gaussian beam relative to a planar beam, along the beam axis. This phase shift occurs due to diffraction in the Gaussian beam. The Guoy phase of the beam at and about the beam waist can be seen in Figure 2.1.

Rayleigh Length (z_0)

The Rayleigh length, z_0 , appears in all of the beam parameter expressions. It is used as a length unit which is universal for all beams. It may be defined in terms of any of the length dependent beam parameters discussed above. Specifically, z_0 is the point at which the $R(z)$ reaches a minimum, $w(z_0) = \sqrt{2}w_0$, and $\xi(z_0) = \pi/4$.

2.1.2. Hermite-Gaussian Beams

The Gaussian beam is not the only solution to the paraxial Helmholtz equation. It is the zeroth order solution of a family of paraboloidal beams known as Hermite-Gaussian, or transverse electromagnetic (TEM_{lm}) modes, where the Gaussian beam is referred to as the TEM_{00} mode. Hermite-Gaussian beams have a different Guoy phase, and a different transverse amplitude profile to the Gaussian beam. The wavefront of a paraboloidal beam matches the curvature of a spherical mirror with a large radius. This is important when arranging a stable resonator, as a wavefront which matches the curvature of the mirror upon which it is incident reflects back upon itself.

¹Discussed further in Chapter 4.

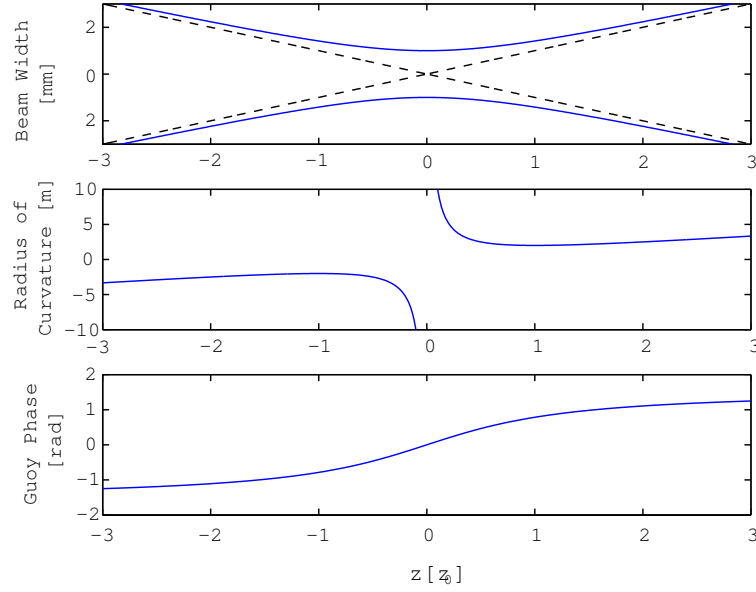


Figure 2.1.: The envelope of a focused Gaussian beam at $W(z)$ (top). The dashed line is the ray optics approximation of the beam envelope. The waist is at the origin and its wavefront is planar at this point, with an infinite radius of curvature $R(0)$ (middle). $\xi(z)$ (bottom) is the phase retardation of the Gaussian beam with respect to a planar wave. It is zero at the origin and approaches $\pm\frac{\pi}{2}$ in the $\pm z$ direction.

2.1.3. Intensity

The beam intensity, in units of W/m^2 , is found by taking the modulus squared of the complex amplitude,

$$I(\mathbf{r}) = |U(\mathbf{r})|^2 = I_0 \frac{w_0^2}{w^2(z)} \exp\left(-2\frac{x^2 + y^2}{w^2(z)}\right) \quad (2.9)$$

where I_0 is the maximum intensity on the optical axis ($x = y = 0$). Within a circle of radius $w(z)$ 86% of the total beam power is contained. Hence, at the waist of the Gaussian beam, the beam power is concentrated over a smaller area, and the intensity at any given transverse point is at a maximum. As is seen in Figure 2.2, the beam intensity drops off as a function of distance from the waist. At one Rayleigh length from the waist, the intensity on the beam axis is half that at the waist. Figure 2.2 also shows the normalised transverse intensity distribution of a Gaussian beam at the waist.

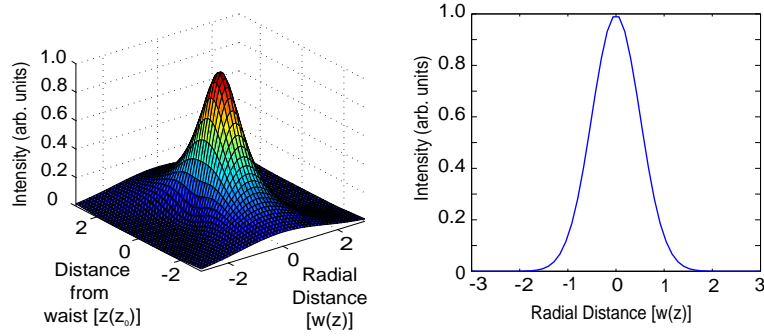


Figure 2.2.: 3D graph (left) of the intensity profile of a TEM₀₀ beam, versus the distance from the waist along the propagation axis. As the beam propagates from the waist, its power spreads out. A normalised cross-section of the beam intensity at the waist is added on the left.

2.2. The Fabry-Perot Resonator

An optical resonator is an optical configuration within which monochromatic light, such as that from a laser, is confined. Optical resonators are also described as multiple beam interferometers. This is because the light contained within an optical resonator will interfere with itself as propagation through the optical configuration takes place. The simplest example of an optical resonator is the Fabry-Perot (FP) resonator, consisting of two mirrors between which light bounces back and forth.

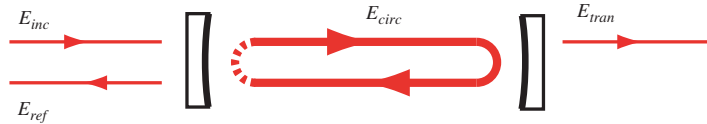


Figure 2.3.: A Fabry-Perot Resonator. The incident field E_{inc} is partially transmitted into the cavity and contributes to the circulating field E_{circ} . Some of this escapes back through the input mirror to interfere with the promptly reflected component of E_{inc} , and the resulting field is known as the reflected field E_{ref} . A portion of the circulating field also escapes through the second mirror and is known as the transmitted field E_{tran} .

Light is injected into a Fabry-Perot resonator via one of the mirrors, provided it has a finite transmission. Once in the cavity, it is confined between the mirrors, with an associated round-trip attenuation due to the transmissivity of the mirrors and the intra-cavity loss. At the time when the round-trip attenuation of the circulating power is equivalent to the amount of light entering the cavity, the cavity enters a steady state. Under these conditions, the field reflected from the cavity E_{ref} , the field circulating within the cavity

E_{circ} , and the field transmitted through the cavity E_{tran} are quantified with respect to the incident beam E_{ref} by the following equations,

$$\frac{E_{circ}}{E_{inc}} = \frac{it_1}{1 - r_1r_2e^{i\phi}e^{-\alpha_{IT}L}} \quad (2.10)$$

$$\frac{E_{ref}}{E_{inc}} = \frac{r_1 - r_2(r_1^2 + t_1^2)e^{i\phi}e^{-\alpha_{IT}L}}{1 - r_1r_2e^{i\phi}} \quad (2.11)$$

$$\frac{E_{tran}}{E_{inc}} = \frac{-t_1t_2e^{i\phi/2}}{1 - r_1r_2e^{i\phi}e^{-\alpha_{IT}L}} \quad (2.12)$$

where

$$\phi = 2kL \quad (2.13)$$

is the phase shift imparted on the beam after a round-trip propagation through a cavity length L , $k = 2\pi/\lambda$ is the wavenumber, r_1 and t_1 are the amplitude reflectivity and transmissivity of the input mirror, respectively, r_2 and t_2 are those for the other mirror, and R_{tran} and R_{ref} are the complex reflection and transmission coefficients for the cavity. The factor of $\exp(-\alpha_{IT}L)$ describes the internal transmission loss, evenly distributed throughout the whole cavity length. These equations follow the convention whereby transmission through a mirror imparts a $\frac{\pi}{2}$ phase shift on the beam. They are derived by solving a set of self-consistent equations for the electric fields [Siegman '86].

2.2.1. Cavity Loss

There are two aspects of cavity loss that are generally considered in the analysis of an optical resonator; internal transmission loss, and mirror loss.

Internal Transmission Loss

The internal transmission loss of a given medium is a measure of the power attenuation of the beam after propagating a given distance within the medium. In the absence of nonlinear interactions, attenuation is caused by two different mechanisms: scattering and absorption. Internal transmission loss is expressed as the imaginary part of the wavenumber k ,

$$k = \frac{2\pi}{\lambda} + i\frac{\alpha}{2} \quad (2.14)$$

where λ is the wavelength of the light, and α is the attenuation coefficient. Consider an electromagnetic wave of complex amplitude $U(\mathbf{r})$, E_0 represents the total electric field, integrated over the spatial dimensions transverse to the direction of propagation, and has units of \sqrt{W} . Propagation by a distance L from its initial state expressed as a phase advance, $\phi = kL$,

$$E = E_0e^{ikL} = E_0e^{i\frac{2\pi L}{\lambda}}e^{-\frac{\alpha}{2}L} \quad (2.15)$$

where E is the total electric field at a longitudinal position L . The oscillating term describes the periodic nature of the electromagnetic wave. The real term, which decreases as a function of distance, describes the amplitude attenuation of the beam. Using Equation 2.15 and $P = E^*E$, α can be derived if the power attenuation over a particular distance is known,

$$P(L) = P(L=0)e^{-\alpha L} \Rightarrow \alpha = \ln \left[\left(\frac{P(L=0)}{P(L)} \right)^L \right] \quad (2.16)$$

Here, $P(L)$ is the power of the beam after propagating a distance L , and $P(L=0)$ is the initial power. In the cavity equations, the loss coefficient has a factor of $1/2$, denoting amplitude attenuation. In this case it has been factored out by the round trip length $2L$.

Mirror Loss

Reflection from the cavity mirrors generally cause most of the light to be reflected, some to be transmitted, and some to be lost from the system. As such, the coefficients associated with the mirror obey the following relation,

$$r^2 + t^2 + \alpha_m = 1 \quad (2.17)$$

where α_m is the mirror loss. It is hidden in the cavity equations by the information provided in the reflection and transmission coefficients.

2.2.2. Cavity Resonance

The amplitudes of the respective fields have a dependence on the relationship between the length of the cavity and the wavelength of the light. For example, the circulating power is at its maximum when the exponential term is unity. This corresponds to a round-trip phase shift (2ϕ) of zero or an integer multiple of π , as the complex exponential has a period 2π . Substitution of $\phi = n\pi$ into Equation 2.13 gives the following,

$$L = \frac{n\pi}{2}\lambda \quad (2.18)$$

This is the longitudinal condition for cavity resonance. It states that the cavity length must be an integer number of half-wavelengths for the field to resonate within. While this defines the point of resonance, resonance effects are also observed for different cavity lengths, or *detunings* about this point. This phenomenon can be explained by considering the interference of the light within the cavity. In a simplified picture, the light within the cavity may be broken up into a chain of discrete packets, entering the cavity via the input mirror. During a round trip of the cavity, one such packet acquires phase, according to the cavity length. It also undergoes attenuation, due to transmission through the mirror and other cavity losses. On returning to the input mirror, it interferes with a second packet of light entering the cavity. The process is repeated an infinite number of times, and the phasors of the respective light packets are vector summed, reaching a steady-state

solution. Figure 2.4 exhibits the vectors sum of the phasors for some different detunings. Because of the wavelength dependent resonance conditions, the FP cavity can be used as a spectrum analyser; only admitting light of a wavelength that satisfies the longitudinal resonance condition stated above. This fact is utilised in the control scheme introduced later in this chapter.

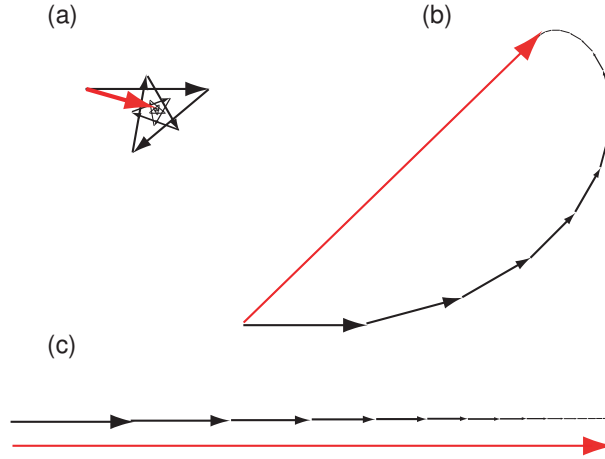


Figure 2.4.: Phasors representing the circulating electric fields of an optical resonator with different detunings. In (a) the cavity is detuned 140° from resonance, and the circulating power (red) is small. In (b) the cavity is closer to resonance, at a detuning of 15° , and exhibits some constructive interference. At this detuning the phasor has an amplitude of approximately $1/\sqrt{2}$, and a relative phase 45° , compared to the resonant cavity (c), where the phasors add constructively, and the circulating power is at its maximum.

2.2.3. Cavity Characterisation

In the undertaking of an experimental characterisation of a FP cavity, there are two useful parameters that are often used; the Full-Width-at-Half-Maximum (FWHM) and the Free Spectral Range (FSR). These are shown in Figure 2.5. The FWHM is defined as the width of the resonance at half transmission. The FSR is defined as the spacing between cavity resonances. It can be derived from the cavity length,

$$\text{FSR} = \frac{c}{2L} \quad (2.19)$$

where c is the speed of light. Because the FSR is a function of the length of the cavity itself, it may be expected that its value should change dynamically as the cavity length is scanned. This is true; however, the length scale over which the cavity length must be scanned in order to map one FSR for a cavity of 10 cm in length with light of a wavelength of $1 \mu\text{m}$ represents a fractional length change of $\Delta L/L = 1/100,000$ and is regarded as

negligible. The equation for the FWHM is,

$$\text{FWHM} = 2\text{FSR} \left[1 - \frac{(1 - r_1 r_2)^2}{2r_1 r_2} \right] \quad (2.20)$$

One FSR corresponds to a cavity length change of $\Delta L = \lambda/2$

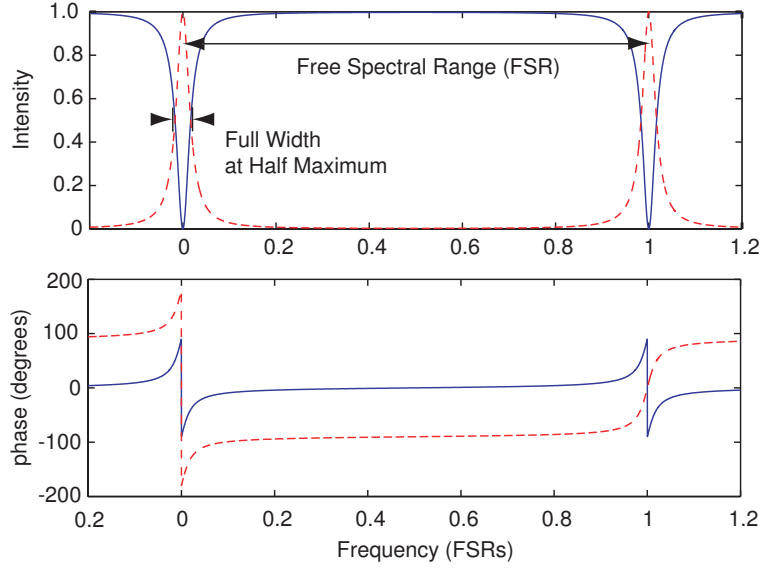


Figure 2.5.: The amplitude (top) and phase (bottom) response of a Fabry-Perot cavity on reflection (blue) and transmission (red dashed), as a function of frequency. Note the phase is not unwrapped for the transmitted field.

The term relating the FWHM and the FSR is known as the finesse, \mathcal{F} ,

$$\mathcal{F} = \frac{\text{FSR}}{\text{FWHM}} \quad (2.21)$$

and may be determined using an approximate version of Equation 2.20²,

$$\mathcal{F} = \frac{\pi \sqrt{r_1 r_2}}{1 - r_1 r_2} \quad (2.22)$$

2.3. Cavity Stability and Mode Matching

A stable beam is set up within the cavity by matching the beam width $w(z)$ and its radius of curvature $R(z)$ with that required at the input mirror to the cavity, at a known position z . This process is known as mode-matching, because it involves matching the parameters of the input beam to that of the cavity eigenmode. The cavity eigenmode can

²See Appendix C

be determined by using the ABCD³ formalism for describing the directional change of a paraxial ray, upon interaction with an optical element. Consider a paraxial beam with beam parameter q incident on an optical element. After interaction with this element, the beam has the new beam parameter q' . This transformation may be described by,

$$q' = \frac{Aq + B}{Cq + D} \quad (2.23)$$

where A, B, C , and D are the elements of the ABCD matrix describing the optic. A and B are dimensionless, while C and D have units of length and inverse length, respectively. Multiple cascaded elements may also be described by one ABCD matrix by taking the reverse product of the individual ABCD matrices.

$$\mathbf{M} = \begin{pmatrix} A & B \\ C & D \end{pmatrix} = \mathbf{M}_n \dots \mathbf{M}_2 \mathbf{M}_1 \quad (2.24)$$

In order to determine the cavity eigenmode, it is required that the beam reproduce itself after one round-trip in cavity. The ABCD matrix for round-trip propagation within a two-mirror cavity, starting at a point z , and propagating in the direction of the second mirror,

$$\mathbf{M} = \mathbf{M}_z \mathbf{M}_{R1} \mathbf{M}_L \mathbf{M}_{R2} \mathbf{M}_{L-z} \quad (2.25)$$

where \mathbf{M}_{R2} is the matrix corresponding to reflection off the second mirror, \mathbf{M}_{R1} is the matrix corresponding to reflection off the input mirror, and \mathbf{M}_{L-z} is the matrix representing the initial propagation to the second mirror, \mathbf{M}_L is the matrix representing the distance between the mirrors, and \mathbf{M}_z represents the distance from the input mirror to the starting point in the cavity.

There are optical configurations that are unable to confine laser beams. A cavity with two convex mirrors is one such example; another is a cavity with two concave mirrors with excessive radii of curvature. The components of this matrix can be used in order to determine the stability criterion of the cavity,

$$\frac{|A + D|}{2} \leq 1 \quad (2.26)$$

This inequality is used before mode-matching calculations are performed in order to determine whether a resonator of a particular length, with mirrors of given curvatures is capable of confining a Gaussian beam. Once the cavity is known to be stable, the components of the matrix are substituted into Equation 2.23. In order to solve this, q is substituted in for q' and a self-sustaining equation results. This may be rearranged into a quadratic equation for $1/q$, with solution,

³For a rigorous discussion of the ABCD matrices, see [Siegman '86]

$$\frac{1}{q} = \frac{D - A}{2B} \pm i \frac{1}{|B|} \sqrt{1 - \left(\frac{A - D}{2}\right)^2} = \frac{1}{R(z)} - i \frac{\lambda}{\pi w^2(z)} \quad (2.27)$$

This equation has two solutions. The allowed solution is such that the imaginary component is negative [Saleh, Teich '91]. Then, by equating the real and imaginary components of each equation, $R(z)$ and $w(z)$ at a point z within the cavity are derived,

$$R(z) = \frac{2B}{D - A} \quad (2.28)$$

$$w(z) = \left(\frac{\lambda}{\pi}\right)^{\frac{1}{2}} \frac{|B|^{1/2}}{(1 - [(A + D)/2]^2)^{1/4}} \quad (2.29)$$

Once these beam parameters are determined, the input laser beam is then able to be matched to them. The requirement to determine the two beam parameters may be fulfilled with the use of at least two lenses prior to the cavity input mirror. This analysis can also be undertaken with the use of the ABCD matrix formalism utilising the matrices for thin lenses⁴. By measuring the beam width at a few points in an arbitrary yet known position, it is possible to determine whether the beam satisfies the required mode-matching conditions of a given cavity.

2.4. Polarisation

In order to understand polarisation, it is useful to treat the laser beam as a wave. Polarisation of a beam refers to the transverse path traced out by end of the electric field vector of the paraxial wave as it propagates, as in Figure 2.6. As there are two degrees of freedom in the plane transverse to the beam, so is it convenient to express any arbitrary elliptical polarisation state as the sum of two basis states. These states are referred to as the transverse magnetic (TM) polarisation, and the transverse electric (TE) polarisation. These are defined with respect to the surface of an optical component of interest; the TE polarisation is defined as the component of the electric field vector that oscillates perpendicular to the optical surface, and the TM mode is defined as the parallel component. The total polarisation state is described by the amplitudes and relative phases of these basis polarisations. A phase offset of $\frac{\pi}{2}$ between the two polarisations of equal amplitude expressed in this basis corresponds to the circularly polarised light shown in Figure 2.6. Linearly polarised light is observed when the two polarisation states have a common phase, or a phase offset of π . A laser beam incident on an optical interface at oblique incidence undergoes polarisation dependent reflection and transmission. For this reason it is often desirable to tailor the polarisation of the beam to suit the experiment being undertaken. It is always possible to either alter the polarisation axis using waveplates, or to alter orientation of the optical device under scrutiny, such that a desired polarisation state is realised.

⁴See Appendix A

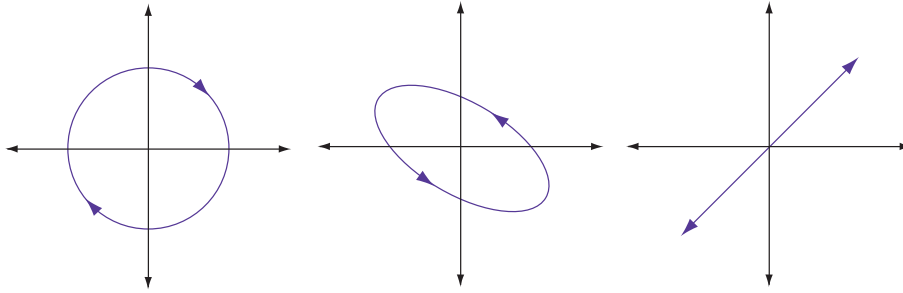


Figure 2.6.: Light exhibiting three different polarisations. Left-circularly polarised light (left), an arbitrary elliptical polarisation (centre) and linearly polarised light at 45° (right).

2.5. Modulation and Cavity Control

The necessity of introducing a control system into this experiment is a consequence of the high finesse cavity that is to be examined. Implementing a control system to achieve what are quite sensitive stability criteria can facilitate the examination of the cavity frequency response; the investigation of which being otherwise difficult and uncertain due to noise coupled into the cavity.

The experiment requires long term observation of the cavity when it is on resonance. The optical cavity in this experiment was expected to have a finesse of the order of 10^3 , corresponding to a FWHM, in terms of cavity length, of $\frac{\lambda/2}{\mathcal{F}}$, where $\frac{\lambda}{2}$. Hence, the FWHM corresponds to a detuning of the order of 10^{-10} m. In order to confine the cavity length perturbations to within this regime, an active control system is required.

The length of the cavity can be controlled using a piezoelectric transducer (PZT). The PZT acts as an actuator, to which one of the mirrors is attached, expanding or contracting according to an applied voltage in order to change the cavity length. It has a range of approximately $1 \mu\text{m}$. It is driven by a proportional integral device (PID) [Yariv '97], which uses information provided by an error signal in order to monitor the deviation of the cavity length from resonance.

The error signal must be zero at the desired operating point of the cavity, and anti-symmetric around it, in order to provide directionally relevant feedback for control.

The PDH locking technique can be used to derive an error signal relevant to the control of optical cavities.

Once the cavity has been stabilised, the cavity may then be interrogated by injecting some component of the light as a swept sinusoid, in order to trace out the power transmission/reflection of the cavity.

2.5.1. Modulation

Modulation is the process whereby a carrier signal, in this case a sinusoid of a frequency ω , is altered by an external waveform. The carrier thus carries the information imparted by this waveform with it. Modulation may be divided into two types, phase modulation (PM) and amplitude modulation (AM). These two modulation regimes form a basis by which any arbitrary modulation can be described. Phase modulation of the beam is necessary

for the implementation of the PDH control scheme, while amplitude modulation is useful in characterising a stabilised high-finesse cavity.

Phase Modulation

Phase modulation at a particular frequency is achieved by periodically altering a beam's optical path, effectively changing the phase with respect to time. A simple phase modulator can be created by altering the position of a mirror with which the beam interacts. However, for high frequency modulation, this is not practical and an electro-optic modulator (EOM) is used. This is a Pockel's cell [Saleh, Teich '91] to which a periodic electric field is applied. The refractive index of the Pockel's cell varies linearly with the voltage of the electric field, which is a sinusoid at the desired frequency, changing the optical path periodically, as required. The effect of this is to couple a portion of the power of the carrier field into phase modulated sidebands. The time dependent complex envelope of the modulated beam is given by,

$$E_{mod} = E_0 e^{i\omega t + i\delta \sin(\omega_m t)} \quad (2.30)$$

where E_0 is the amplitude of the electric field of the beam prior to modulation, E_{mod} is the electric field of the modulated beam, ω is the frequency of the carrier, ω_m the modulation frequency, and δ the modulation depth. The modulation depth corresponds to the portion of the power transferred to the sidebands. Equation 2.30 may be re-expressed, to first order, as

$$E_{mod} = E_0 e^{i\omega t} [(J_0(\delta) + J_1(\delta) (e^{i\omega_m t} - e^{-i\omega_m t}))] \quad (2.31)$$

which explicitly shows the first order sidebands which are found on either side of the carrier. In this case, sine phase modulation has been examined. A similar derivation of cosine phase modulation gives the same result with a phase offset of $\frac{\pi}{2}$ in the sideband terms. Sine modulation and cosine modulation produce the same effect, and differ only by the arbitrary time at which $t = 0$ is defined.

Figure 2.8 exhibits a phasor representation of relationship between the carrier and the sidebands. This figure represents a snapshot in time. The plane transverse to the frequency axis is the complex plane. The length of a vector represents the amplitude of the electric field, and the angle in the complex plane represents its phase. Rotating the reference frame at the frequency of the carrier, the lower sideband regresses in phase as time advances, while the upper sideband advances in phase. Hence, at any time, the amplitude quadrature (real) projections of these two phasors exhibit destructive interference, while the phase quadrature (imaginary) projections exhibit constructive interference.

Amplitude modulation

Amplitude modulation is the process of modulating the amplitude of the electromagnetic wave. This can be achieved with the use of an EOM that exhibits electrically induced

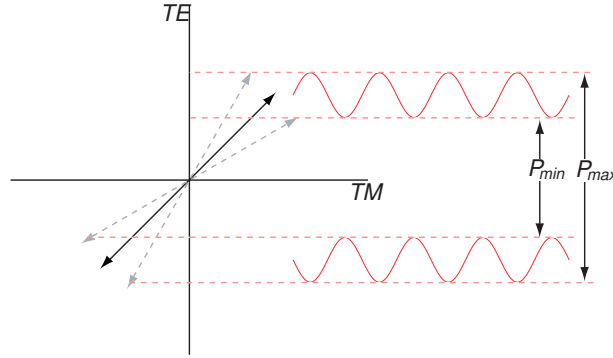


Figure 2.7.: The polarisation vector after passing through an amplitude modulator and quarter-wave plate. The component of the vector transmitted through a polariser oriented along the x-axis changes periodically over time by electrically induced birefringence in the amplitude modulator.

birefringence. The effect of this is to alter the relative path lengths of the polarisation states as a function of time. Linearly polarised light is incident on the axes of birefringence at an angle of 45 degrees, such that half of the light is projected onto one of the birefringence axes, and half on the other. Half the light is retarded dynamically with respect to the other half, and the polarisation vector, referring to Figure 2.6, alters its position periodically. The light is then passed through a quarter wave plate, which is positioned prior to a polariser. The projection of the polarisation vector onto the axis of the polariser creates modulation of the transmitted beam amplitude, as this projection varies with time. The quarter-wave plate is positioned in order to orient the polarisation at 45 degrees to the polariser, such that the maximum change in projection is observed over a given modulation period. The time dependent complex envelope of an amplitude modulated beam is given by,

$$E_{mod} = E_0 e^{i\omega t + \delta \sin \omega_m t} \quad (2.32)$$

This time, modulation of the real component of the exponential is observed. The first order approximation is,

$$E_{mod} = E_0 e^{i\omega t} [(J_0(\delta) + J_1(\delta) (ie^{-i\omega_m t} - ie^{i\omega_m t})] \quad (2.33)$$

Here, the sidebands have a different phase relationship with respect to each other, such that their projections onto the phase quadrature always destructively interfere, while constructive interference is observed in the amplitude quadrature.

2.5.2. The Pound-Drever-Hall Locking Technique

PDH locking requires phase modulation of the input beam. The modulation frequency is chosen to be much greater than the cavity linewidth. When the carrier is at or near the

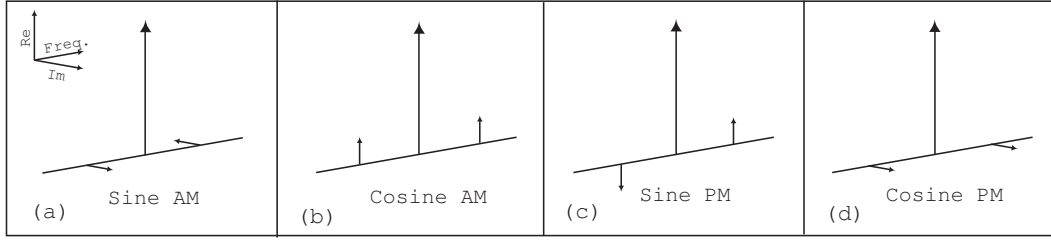


Figure 2.8.: Cosine and sine amplitude and phase modulation. The phase relationship between the sidebands and the carrier at one snapshot in time is shown. The phase of the sidebands are represented by their projection onto the imaginary axis, and their amplitude is the real-axis projection.

resonance frequency of the cavity, it obtains the cavity phase response. The sidebands are well outside the cavity resonance, and are promptly reflected, obtaining no phase shift. The relative phase shift between the sidebands and the carrier introduces an amplitude modulation component, or a beat pattern, which is able to be detected by the photodiode. The power reflected from the cavity at ω_m is given by [Black '00],

$$P_{ref} = 2\sqrt{P_c P_s} \{ \Re[F(\omega)F^*(\omega + \omega_m) - F^*(\omega)F(\omega - \omega_m)] \cos \omega_m t \dots + \Im[F(\omega)F^*(\omega + \omega_m) - F^*(\omega)F(\omega - \omega_m)] \sin \omega_m t \} \quad (2.34)$$

where $F(\omega)$ is the complex reflectivity of the cavity at a frequency ω , and P_c and P_s are the powers in the carrier and sidebands, respectively. A similar derivation can be made for the transmitted beam.

The signal is then detected, and mixed with a fraction of the signal driving the phase modulator, or the local oscillator. Hence, the detected signal is converted into two components, one at DC, and one oscillating at $2\omega_m$. The relative phase of the local oscillator and the detected signal determines the degree to which either the real or imaginary component is extracted. For a modulation frequency outside the cavity linewidth, the sidebands are totally reflected: $F(\omega \pm \omega_m) \approx -1$, such that only the imaginary component of Equation 2.34 survives. Therefore, it is necessary to adjust the demodulation phase such that this term is maximised, to ensure that the largest possible error signal is recovered. The mixed signal is then passed through a low-pass filter in order to eliminate the $2\omega_m$ component. That which remains is the error signal ϵ

$$\epsilon = -2\sqrt{P_c P_s} \Im[F(\omega)F^*(\omega + \omega_m) - F^*(\omega)F(\omega - \omega_m)] \quad (2.35)$$

The error signal is plotted in Figure 2.9. In the presence of a disturbance, the error signal assumes a nonzero value. It is sent to the servo, which uses the information to drive the PZT such that the error signal return to zero, corresponding to cavity resonance.

2.5.3. Cavity Interrogation with an Amplitude Modulated Beam

To accurately map out the frequency response of the cavity, and therefore the FWHM, an AM transfer function of the cavity was measured. This was done with the cavity locked

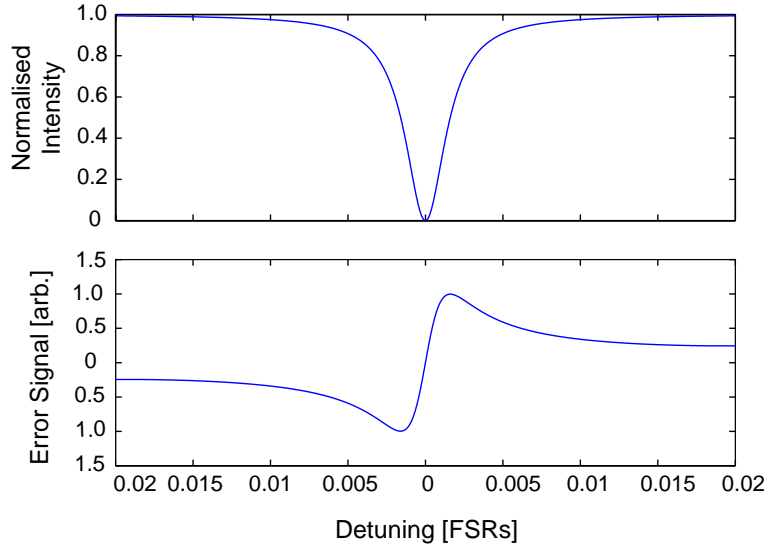


Figure 2.9.: The reflected intensity (top) and error signal (bottom) for a 50 cm long two mirror cavity with $R_1 = R_2 = 0.99$, a modulation frequency of 10 MHz, and a modulation depth of 0.1.

to resonance as follows: The incident beam was amplitude modulated, with a swept sine signal, applied to a broadband amplitude modulator. The transmitted power, which contained this AM signal, attenuated by the cavity frequency response was measured. This transmitted signal was compared to the driving signal using a network analyser, giving the frequency response of the cavity.

2.6. Summary

This chapter has presented the requisite information for the implementation of the experiment. Knowledge of the properties of the Gaussian beam was used in conjunction with the mode-matching and optical resonator theory in order to build the two-mirror CFM cavity. The laser beam incident on this cavity was polarised in order that the polarisation sensitive CFM exhibit maximum reflectivity, requiring a familiarity with the nature of polarisation, as presented. Both phase modulation and amplitude modulation were described; the former due to its used in the PDH control technique, and the latter due its use in probing the cavity response. The control theory presented was implemented in the experiment in order to maintain cavity length stability, such that the cavity could be interrogated using swept AM sidebands.

Chapter 3.

Mirror Design

The objective of this project was to design a highly reflective mirror without the use of optical coatings. This chapter introduces an original design for such a Coating-Free Mirror (CFM). This design is based on the concepts of total internal reflection (TIR) and Brewster's angle. Accordingly, the chapter begins with explanations of these concepts. Next, this theory is implemented in the design concept, which is then refined by calculating appropriate dimensions. The expected reflectivity of the mirror is then estimated based on the dimensions and material parameters, and the cavity equations for a two mirror cavity of a CFM and a conventional mirror are presented by analogy with a FP cavity.

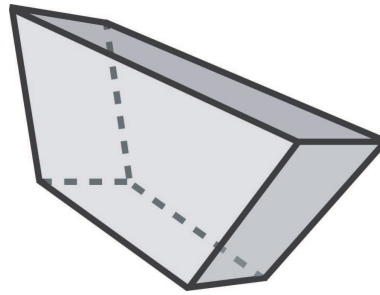


Figure 3.1.: Perspective drawing of the CFM.

3.1. Electromagnetic Waves in matter

3.1.1. Snell's Law and TIR

The change in trajectory of an electromagnetic wave passing through a dielectric interface is described by *Snell's Law*, which arise from Maxwell's equations and electromagnetic boundary conditions,

$$\frac{\sin \theta_t}{\sin \theta_i} = \frac{n_i}{n_t} \quad (3.1)$$

where θ is measured with respect to the interface normal, n is the refractive index of a given medium, and the subscripts i and t refer to the incident and transmitted rays,

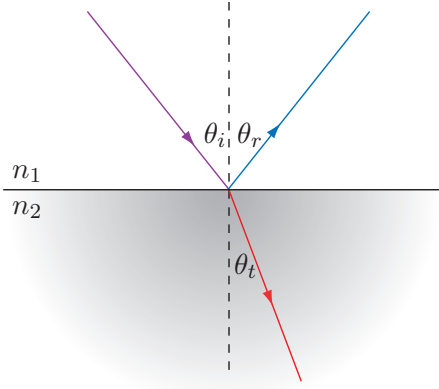


Figure 3.2.: The trajectories of the transmitted (red) and reflected (blue) part of a beam incident (purple) at an angle θ_i with respect to the normal of an interface between dielectrics of refractive index n_1 and n_2 , respectively, as described by Snell's Law.

respectively, and r will refer to the reflected. The angle of the reflected beam is equal to the angle of the incident beam, ($\theta_i = \theta_r$). The incident, reflected, and transmitted rays are all coplanar.

When passing from one medium into another of a lower refractive index, there is an angle above which Equation 3.1 would be required to satisfy $\sin \theta_t > 1$. Hence, in this case, the solution for θ_t is imaginary, and the beam is totally reflected¹. In this way the phenomenon referred to as 'total internal reflection' arises from Snell's Law. The angle of incidence above which TIR occurs is known as the critical angle, θ_c ,

$$\theta_c = \sin^{-1} \frac{n_t}{n_i} \quad (3.2)$$

In this case, $n_i > n_t$.

3.1.2. The Fresnel Equations

In the following, a set of equations known as the Fresnel equations [Saleh, Teich '91] is introduced in order to describe the power of the beam transmitted T through, and the beam reflected, R , from a dielectric interface. These powers depend on the angle and the polarisation state of the incident beam.

$$R_{\perp} \equiv \frac{P_{r\perp}}{P_{i\perp}} = \left(\frac{\alpha - \beta}{\alpha + \beta} \right)^2 \quad T_{\perp} \equiv \frac{P_{t\perp}}{P_{i\perp}} = \alpha\beta \left(\frac{2}{\alpha + \beta} \right)^2 \quad (3.3)$$

$$R_{\parallel} \equiv \frac{P_{r\parallel}}{P_{i\parallel}} = \left(\frac{\alpha\beta - 1}{\alpha\beta + 1} \right)^2 \quad T_{\parallel} \equiv \frac{P_{t\parallel}}{P_{i\parallel}} = \alpha\beta \left(\frac{2}{\alpha\beta + 1} \right)^2 \quad (3.4)$$

¹It is noteworthy that under certain circumstances, TIR can be frustrated. See [Albiol '92] for a discussion of 'Frustrated Total Internal Reflection'

where,

$$\alpha = \left(\frac{\cos \theta_t}{\cos \theta_i} \right) \quad \beta = \frac{n_t}{n_i}$$

where R_{\perp} and T_{\perp} are the respective reflected and transmitted powers of the TM polarised component of the incident light; R_{\parallel} and T_{\parallel} are the corresponding for the TE polarised component. Figure 3.4 shows the power of a TM polarised beam, incident on an interface between dielectrics of given refractive indices, as a function of the incident angle. Figure 3.3 shows the case for TE polarisation. Total Internal Reflection is evident in both polarisations, and the critical angle can be deduced graphically, at around 43° for $n_t = 1$, the refractive index of air, and $n_i = 1.45$, the refractive index of fused silica, the material used for the CFM.

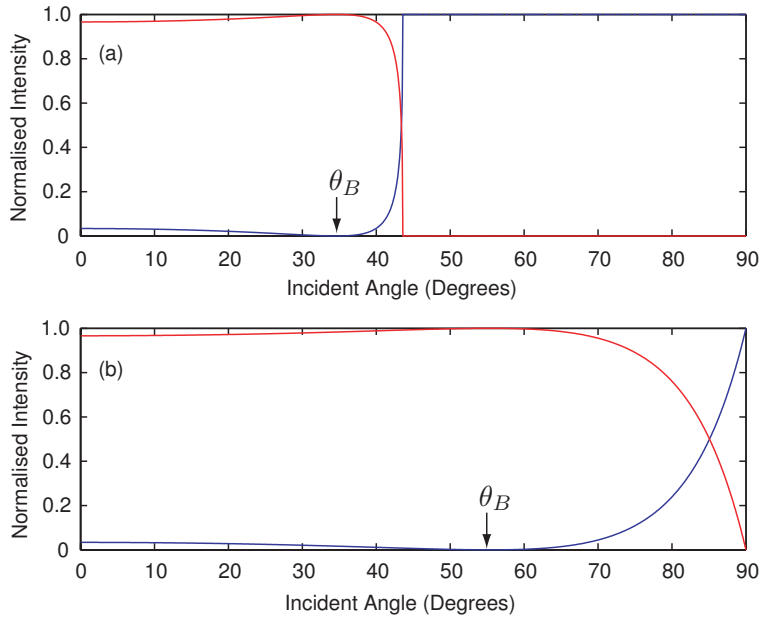


Figure 3.3.: The transmitted (red) and reflected (blue) intensities of a TM polarised beam incident on an interface between dielectrics with (a) $n_i = 1.45$, $n_t = 1$ and (b) $n_i = 1$, $n_t = 1.45$, as a function of the angle the incident beam makes with respect to the interface normal.

3.1.3. The Brewster Angle

Comparison of Figure 3.4 with Figure 3.3 illustrates that the reflected power of each polarisation has a strong, yet different, dependence on the angle of the incident beam. The TE polarised electromagnetic wave exhibits a nondecreasing reflectivity as θ_i is increased. For TM polarised light, however, the reflectivity drops to zero at a particular angle. This angle is known as the Brewster Angle, θ_B , at which the reflected beam (blue) in Figure 3.2

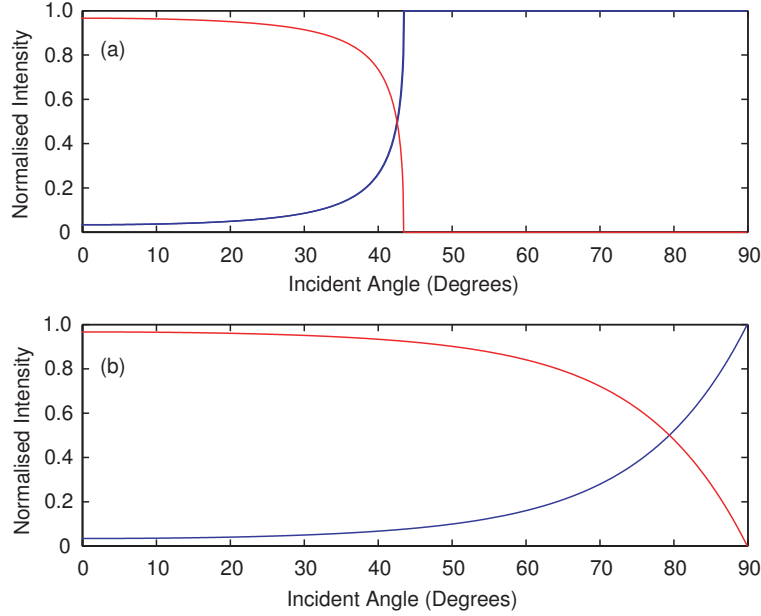


Figure 3.4.: The transmitted (red) and reflected (blue) intensities of a TE polarised beam incident on an interface between dielectrics with (a) $n_i = 1.45$, $n_t = 1$ and (b) $n_i = 1$, $n_t = 1.45$, as a function of the angle the incident beam makes with respect to the interface normal.

disappears, leaving only the transmitted beam (red). The Brewster angle is given by,

$$\tan \theta_B = \frac{n_t}{n_i} \quad (3.5)$$

This is the angle at which the addition of the incident angle and the refracted angle add up to exactly 90° . The Brewster Angle is often utilised in order to create maximally transmissive optics.

3.2. Coating-Free Mirror Concept

In order to reflect light with a minimum of loss, we use a glass substrate whose surfaces exist as a boundary between two dielectrics, taking advantage of the phenomenon of TIR. At this point there are two important aspects of this premise that must be accounted for. Firstly, in order to experience TIR, the light must be propagating towards a medium of a lesser refractive index, and must also be incident on the dielectric boundary at an angle greater than θ_c . Secondly, the light must be coupled into and out of this medium, with negligible loss. The Brewster angle provides a perfect entry condition for this purpose, with the advantage that the process is reversible; a perfectly retro-reflected beam leaves the CFM at the Brewster angle also. See Figure 3.4 to see how the Brewster angle changes depending on the medium from which the light is incident on the interface.

The idea is to couple a TM polarised beam into a medium with a sufficiently high refractive

index, via the Brewster angle, such that it can reflect the beam back. The light is reflected via TIR from two surfaces. Due to a straightforward geometrical argument, it is clear that the angle between these two surfaces must be at least $2\theta_c$, to ensure that the beam can be reflected off both surfaces under TIR. Under the assumption that this is a 90° angle, we arrive at the following condition, derived from Equation 3.2 with the condition that $\theta_c \leq 45^\circ$. Also $n_1 = n_{air} = 1$, $n_2 = n_{dielec}$,

$$n_{dielec} \geq \sqrt{2} \quad (3.6)$$

From Figures 3.4 and 3.3 we see how important it is that the incident light have the correct polarisation. For TE polarised light, the in-coupling and out-coupling losses are both approximately 12.5% at the Brewster angle.

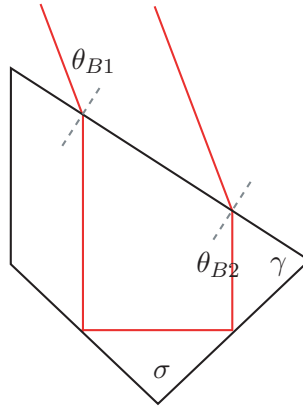


Figure 3.5.: The coating free mirror concept.

In Figure 3.5, γ is given by $45^\circ + \theta_{B2}$, σ is 90° . We see that the Brewster window is oriented with respect to the corner so that light incident at the Brewster angle refracts directly towards it. Theoretically, if the CFM is aligned correctly with respect to the incident beam, and the incident beam is perfectly polarised, this reflector should suffer loss only due to internal transmission.

3.3. Design for Experiment

The choice of material for the CFM was suprasil 1 grade fused silica (SiO_2). Fused silica has a refractive index $n_{\text{SiO}_2} = 1.45$. Fused silica is the choice of material for the current generation of gravitational wave detectors, and will also feature in Advanced LIGO. This is because fused silica has a very low transmission loss. The loss of the fused silica in our experiment is quoted as² 0.999962 cm^{-1} .

²Specification for Suprasil 1 fused silica, provided by PhotonLaserOptik, Gmbh.

3.3.1. CFM Size

The coating-free mirror design was created by

In this experiment, a traveling wave cavity will be created using the CFM and a conventional mirror with reflectivity 99.95%, and radius of curvature $R = 0.5$ m. As discussed in the introductory chapter, the size of the CFM. is minimised in order to reduce its moment of inertia. This is important for sensitivity to quantum fluctuations in radiation pressure when designing an experiment to measure the standard quantum limit. To determine an appropriate CFM size for this experiment, the expected size of the beam waist in the cavity, w_0 , is calculated. The model used is a close approximation of the CFM cavity; a Fabry-Perot cavity with a flat mirror and a mirror with radius of curvature $R = 0.5$.

$$w_0 = \sqrt[4]{\frac{\lambda^2(L^2 - LR)}{\pi^2}} \quad (3.7)$$

gives the beam waist radius w_0 in the cavity as a function of cavity length L . The flat mirror is an approximation of the CFM with its flat TIR surfaces. We can use this equation to calculate the waist size for all stable cavity lengths. From it, we find the maximum possible waist radius is $291 \mu\text{m}$ at a cavity length of 25 cm. From this, an estimate of the required CFM size could be made. In Figure 3.6b, the cross-section of the reflective surfaces, x , as seen by the incoming and outgoing beams, is shown. For a Gaussian beam, the fraction of the total light power passing through a circle of radius r perpendicular and coaxial to the beam is,

$$\frac{P}{P_{tot}} = 1 - \exp\left[-\frac{2r^2}{w^2(z)}\right] \quad (3.8)$$

where $w(z)$ is the radius of the beam at a point z away from the waist. From Figure 3.6a we can see that a negligible amount of beam power lies outside a circle of radius $3w_0$. The Rayleigh range for a beam of radius $291 \mu\text{m}$ is approximately 38 cm. With this knowledge it can be said that the waist is near enough, in terms of the Rayleigh range, to the Brewster windows to be a good approximation of the beam size there. Hence, the assumed beam radius at this point is $w = 300 \mu\text{m}$. From Figure 3.6b, the effective aperture required for input and output of the beam, $x \times \frac{x}{2}$, must be at least $12w_0 \times 6w_0$ (3 beam diameters per beam in each dimension), or $1.8 \text{ mm} \times 3.6 \text{ mm}$. In addition to this length, approximately 2.4 mm was added to x , in order to allow for some alignment freedom when conducting the experiment. Therefore $x = 6 \text{ mm}$ was the specified characteristic length for the CFM. It is this length from which all others will be derived. From Figure 3.6b, the height of the CFM is 3 mm .

Before the dimensions of the CFM are worked out explicitly, some changes need to be made to the CFM model, in order to make it suitable for the experiment.

3.3.2. Corner Angle

In order to create an optical cavity comprising the CFM and conventional mirror, it is required that the incident and reflected beams cross at the point at which the conventional

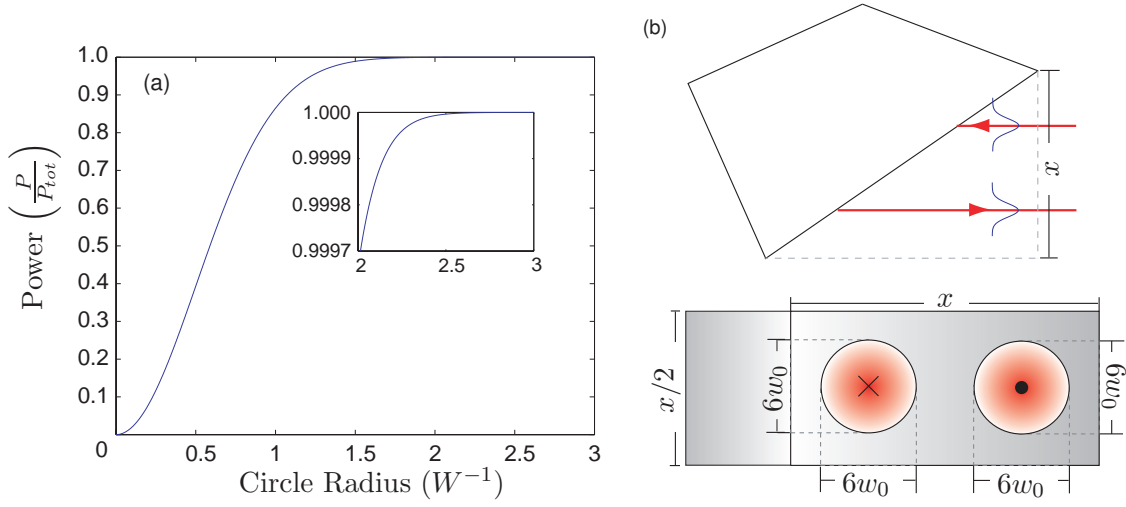


Figure 3.6.: (a) The ratio of the power of a gaussian beam, carried within a circle of radius r in the transverse plane, where r is expressed in terms of the beam radius $w(z)$. (b) Top: The dotted line is the size of the reflecting surface in the transverse plane to the beam. Bottom: The effective size of the front face window is larger than the minimum required $6w_0 \times 12w_0$, in order to relax what would otherwise be very strict alignment conditions.

mirror is placed. Thus, the corner angle is reduced by a small amount δ , as in Figure 3.7a. The characteristic length, x , which defines the size of the CFM remains the same, and the lengths of the other sides adjust accordingly to accommodate any angular changes. The TIR condition for the reduced corner angle is found in much the same way as in Equation 3.6. To first order,

$$n_{SiO_2} \gtrsim \frac{\sqrt{2}}{1 - \frac{\delta}{2}} \quad (3.9)$$

derived from the condition that $\theta_c \leq 45^\circ - \frac{\delta}{2}$.

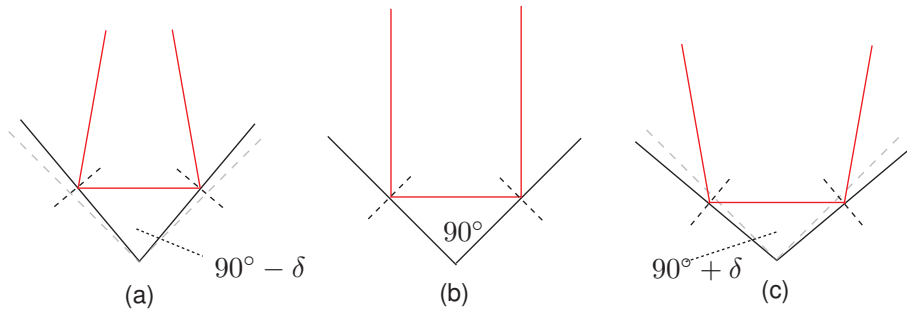


Figure 3.7.: Trajectory of light incident on the corner when its angle is (a) less than 90° , (b) equal to 90° , (c) greater than 90° .

Solving for δ in Equation 3.9 we find, $\delta \lesssim 2.8^\circ$. Therefore, if δ is greater than 2.8° , TIR at the reflective surfaces breaks down.

There are two main considerations at this point. The greater δ is, the greater the loss of the CFM; for even when optimally aligned, each beam will deviate from the Brewster angle by δ , and thus introduce loss, given by Equations 3.3. Optimal alignment refers to alignment of the CFM such that the beam is incident on each reflecting surface with the same angle. However, the smaller δ is, the greater the distance from the corner reflector to the beam-crossing point. The stability criterion for a two-mirror cavity with a flat mirror says,

$$L \leq R \quad (3.10)$$

where L is the length of the cavity, and R is the radius of curvature of the conventional mirror. Therefore, δ needs to be kept sufficiently high such that the length of the cavity does not exceed R .

The following equation is used to derive the length from the Brewster window to the HR mirror, as a function of δ ,

$$L = \frac{1.23 - 4.16\delta}{\theta_{B1} - \sin^{-1} [n_{\text{SiO}_2} \sin(\theta_{B2} - \delta)]} \quad (3.11)$$

derived by geometrical arguments and Snell's law. This was used in Figure 3.8, and is particular to this CFM design. The distance of propagation through the CFM needs to be added to this value in the derivation of the cavity length.

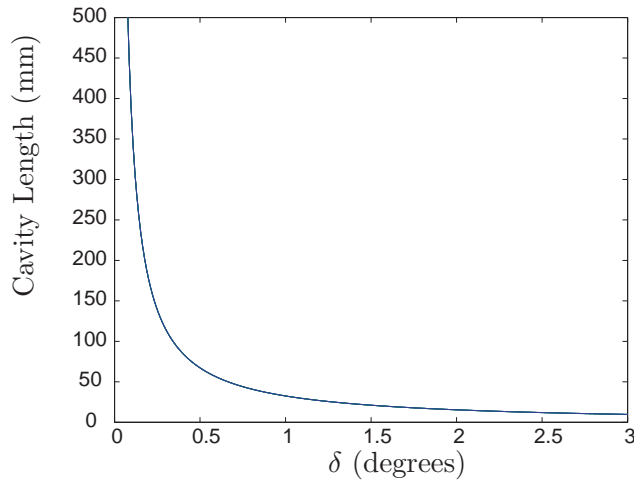


Figure 3.8.: The cavity length as a function of the change in corner angle δ .

The value given to the manufacturer was $\delta = 0.5^\circ \pm 0.2^\circ$. The large allowed error of 0.2° was provided to allow for the unknown manufacturing process. These values correspond to a range of L between 50 mm and 115 mm, with a specified length of around 70 mm.

Extra loss introduced due to the deviation from the Brewster angle at the front window is able to be accounted for using the theoretical models. With the value for δ , the design of the corner cube to be used this experiment is complete. Figure 3.9 shows the resulting dimensions of the CFM, and beam trajectories for optimal alignment. There are finite losses from each window, and the primary reflected beams are denoted Beam 1 and Beam 2 in the remainder of the thesis.

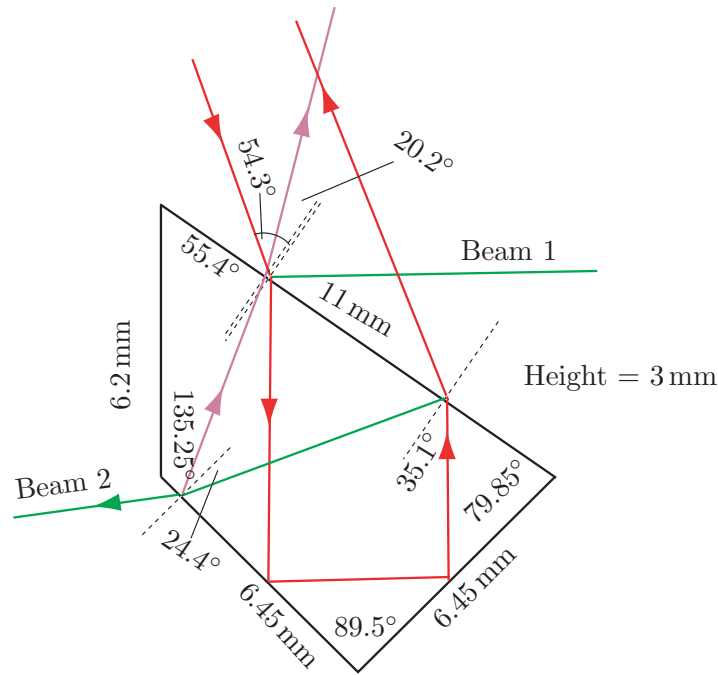


Figure 3.9.: The dimensions of the CFM design for this experiment. The input beam is aligned such that each reflection at the back surfaces is incident at the same angle. The reflections of the beam are also shown; Primary reflections are shown in green, and secondary reflections are in purple.

A calculation based on the CFM dimensions, and the known density of fused silica. $\rho = 2.65 \text{ g/cm}^3$, gave a predicted CFM weight of 0.43 g. This fulfills the requirement that the CFM have a weight below 0.5 g.

3.3.3. CFM Reflectivity

With the corner angle slightly reduced, the beams no longer hit the front face at exactly the Brewster angle. For optimal alignment, the angle between the incoming beam inside the CFM and the norm of front face is 35.1° . Using Snell's Law, this gives us an incident angle of 54.3° , which corresponds to a loss $L_1 = 0.00011$. From the specified dimensions of the CFM, the distance the beam travels within the fused silica is approximately $L = 1.5 \text{ cm}$. The internal transmission loss coefficient α can first be worked out by using the

provided loss per centimetre, and Equation 2.15, according to the internal transmissivity, specified by the manufacturer, of 0.999962cm^{-1} ,

$$\alpha(\text{cm}^{-1}) = -\ln(0.999962) \quad (3.12)$$

which gives a loss $L_2 = 0.00006$. The outgoing beam hits the front face of the CFM at an angle 34.1° . From the Equations 3.4, this gives a loss due to reflection $L_3 = 0.00010\%$ at the output Brewster window. Hence, the total reflectivity of the mirror is,

$$\frac{P_r}{P_i} = (1 - L_1)(1 - L_2)(1 - L_3) = 0.99973 \quad (3.13)$$

where P_i is the power of the beam entering the CFM and P_r is the power after exiting. Thus, the expected power reflectivity of the mirror is 99.97%. Assumptions made here are: negligible loss at the TIR windows, and perfect alignment in the beam transverse plane.

3.3.4. CFM Rotation

The reflectivity of the CFM has an angular dependence, which is contained in the angular dependence of the Fresnel equations; as the incident beams move away from the Brewster angle, a greater fraction of the power is reflected from the front face of the CFM. This examination of the reflectivity as a function of the CFM rotation will form the basis for an experimental observation of this effect. The axis of rotation for the CFM is the point at which the light enters the CFM. An equivalent way to think about this is to change the angle of the incident beam. Figure 3.10 shows beam trajectories for five CFM rotation angles.

To examine the reflectivity of the CFM for an arbitrary incident angle, the fraction of the reflected beam power with respect to the incident beam power is considered using the following equation,

$$\frac{P_r}{P_i} = \frac{16\alpha_1\alpha_2 0.999962^{1.52}}{(\alpha_1 + \beta_1)^2(\alpha_2 + \beta_2)^2} \quad (3.14)$$

where,

$$\alpha_1 = \frac{\sqrt{1 - \beta_2^2 \sin^2 \theta_1}}{\cos \theta_1}$$

$$\alpha_2 = \frac{\sqrt{1 - \beta_1^2 \sin^2 \theta_2}}{\cos \theta_2}$$

$$\beta_1 = \frac{1}{1.45}$$

$$\beta_2 = 1.45$$

$$\theta_1 = 54.3^\circ - \rho$$

$$\theta_2 = \sin^{-1}(\beta_1 \sin \theta_1) + 2\delta$$

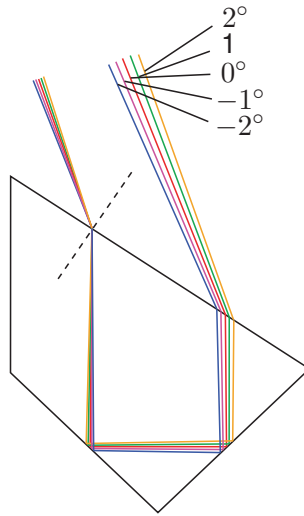


Figure 3.10.: Beam trajectories as the CFM is rotated from the point of optimal alignment. Breakdown of TIR occurs if the rotation is approximately larger than 5° either way.

where the subscripts 1 and 2 refer to 1^{st} and 2^{nd} transmission through the front face, respectively. Making the appropriate substitutions, the equation for the transmitted power depends only on the rotation angle ρ . When $\rho = 0$, we return to the conditions by which Equation 3.13 was derived. In Figure 3.11, Equation 3.14 has been used to determine the reflectivity of the CFM for each of the beams in Figure 3.10.

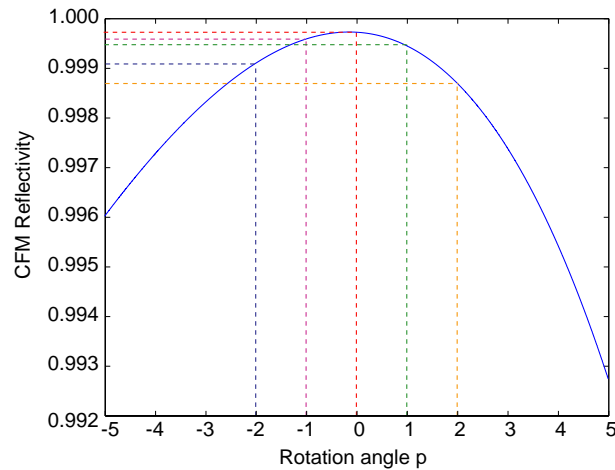


Figure 3.11.: The reflectivity as a function of CFM rotation ρ , centered around the optimum injection angle for our CFM design of 54.3° . The reflected powers of the beams in Figure 3.10 are also shown by the dotted lines, which are colour coded according to the corresponding rays. The profile is asymmetric due to the asymmetry of the power Fresnel equations about the Brewster angle.

3.4. CFM Cavity Equations

The amplitude transmission and reflectivity coefficients required in the derivation of the cavity equations are defined as follows,

$$r_i = \sqrt{R_i} \qquad t_i = \sqrt{T_i} \qquad (3.15)$$

The power reflectivity of the mirror was defined in Equation 3.14, and shall be denoted R_2 from hereon,

$$R_2 = \frac{P_r}{P_i} = \frac{16\alpha_1\alpha_2 0.999962^{1.52}}{(\alpha_1 + \beta_1)^2(\alpha_2 + \beta_2)^2} \qquad (3.16)$$

Substitution into Equation 3.15, with the addition of a factor that may be altered in order to account for loss at the two reflective windows, r_{TIR}^2 , gives

$$r_2 = r_{TIR}^2 \frac{4\sqrt{\alpha_1\alpha_2} 0.999962^{0.76}}{(\alpha_1 + \beta_1)(\alpha_2 + \beta_2)} \qquad (3.17)$$

Which may then be used to substitute in the Equations for the FP cavity defined earlier. This is valid for the circulating field E_{circ} , and the reflected field E_{ref} ,

$$\frac{E_{circ}}{E_{inc}} = \frac{it_1}{1 - r_1 r_{TIR}^2 \left(\frac{4\sqrt{\alpha_1\alpha_2} 0.999962^{0.76}}{(\alpha_1 + \beta_1)(\alpha_2 + \beta_2)} \right) e^{i\phi}} \qquad (3.18)$$

$$\frac{E_{ref}}{E_{inc}} = \frac{r_1 - r_{TIR}^2 \left(\frac{4\sqrt{\alpha_1\alpha_2} 0.999962^{0.76}}{(\alpha_1 + \beta_1)(\alpha_2 + \beta_2)} \right) (r_1^2 + t_1^2) e^{i\phi}}{1 - r_1 r_{TIR}^2 \left(\frac{4\sqrt{\alpha_1\alpha_2} 0.999962^{0.76}}{(\alpha_1 + \beta_1)(\alpha_2 + \beta_2)} \right) e^{i\phi}} \qquad (3.19)$$

where the internal transmission loss of the mirror was considered to be the only source of this loss in the otherwise free-space cavity.

The transmitted field is defined differently due to the nature of the CFM. There are four points of transmission; one from the reflection as the beam passes into the CFM (Beam 1), one from the reflection as the beam passes out from it (Beam 2), and one each due to an unknown amount of loss at the reflectors. The powers of beams 1 and 2, P_{B1} and P_{B2} respectively, are able to be characterised from the theory, using the known circulating power, along with the reflection at each point as defined by the power fresnel equations,

$$P_{B1} = \left(\frac{\alpha_1 - \beta_1}{\alpha_1 + \beta_1} \right)^2 P_{circ} \qquad (3.20)$$

$$P_{B2} = R_{TIR}^2 \alpha_1 \beta_1 \left(\frac{2}{\alpha_1 \beta_1 + 1} \right)^2 \left(\frac{\alpha_2 - \beta_2}{\alpha_2 + \beta_2} \right)^2 P_{circ} 0.999962^{1.52} \qquad (3.21)$$

where P_{circ} is the circulating power in the cavity, found from Equation 3.18 and $P = |E|^2$. With the powers of the two beams defined by theory, comparison can be made to a measured value in order to infer information regarding the circulating field as the CFM is rotated.

Chapter 4.

Experimental Setup and Results

In order to characterise the CFM reflectivity, it was included in a two-mirror cavity, along with a conventional spherical mirror. This chapter discusses the process of setting up the experiment, and presents the data recorded. It begins with a general description of the experimental layout, followed by relevant information regarding the setup of the cavity. This includes a characterisation of the mirror spatial dimensions, providing the means to calculate the cavity length before mode-matching of the interrogating laser beam. Alignment of the cavity is described, as the non-conventional nature of the mirror requires some special consideration.

With the successful alignment of the cavity, data recorded by scanning the length of the cavity provided a means for characterisation of the CFM reflectivity. These measurements were marred by acoustic noise, requiring the use of cavity stabilisation. Results pertaining to the successful implementation of the control system are then included, along with a description of the process.

With cavity stabilisation in place, a detailed interrogation of the cavity frequency response could be undertaken using amplitude modulated sidebands. This was used to find the rotational alignment of the CFM that yielded the highest reflectivity. Once this was obtained, the rotational alignment was iteratively altered to map out the resulting reflectivity of the CFM as a function of rotation. Comparison of the experimentally derived reflectivity with that predicted theoretically was used to infer information not included in the model.

Following this, an examination of the circulating power in the cavity under CFM rotation was undertaken by measuring the change in the power of the beam reflected from the front face, in order to make a comparison with the theoretical model. This was done in order to infer information about the sensitivity of the cavity to misalignment for a fixed input beam alignment.

4.1. Experimental Layout

A schematic diagram of the experimental layout is shown in Figure 4.1. The laser used in this experiment was an Innolight Mephisto M500 neodymium-doped yttrium-aluminium-garnet (Nd:YAG) laser at 1064 nm. It is passed through a polarising beamsplitter, for correct polarisation alignment required at the phase modulator. A phase modulator and an amplitude modulator are used for cavity control and interrogation, respectively. The amplitude modulator works in tandem with the Glan-Taylor prism (GT prism), which coupled the light to the TM polarisation required for the CFM cavity. Two steering

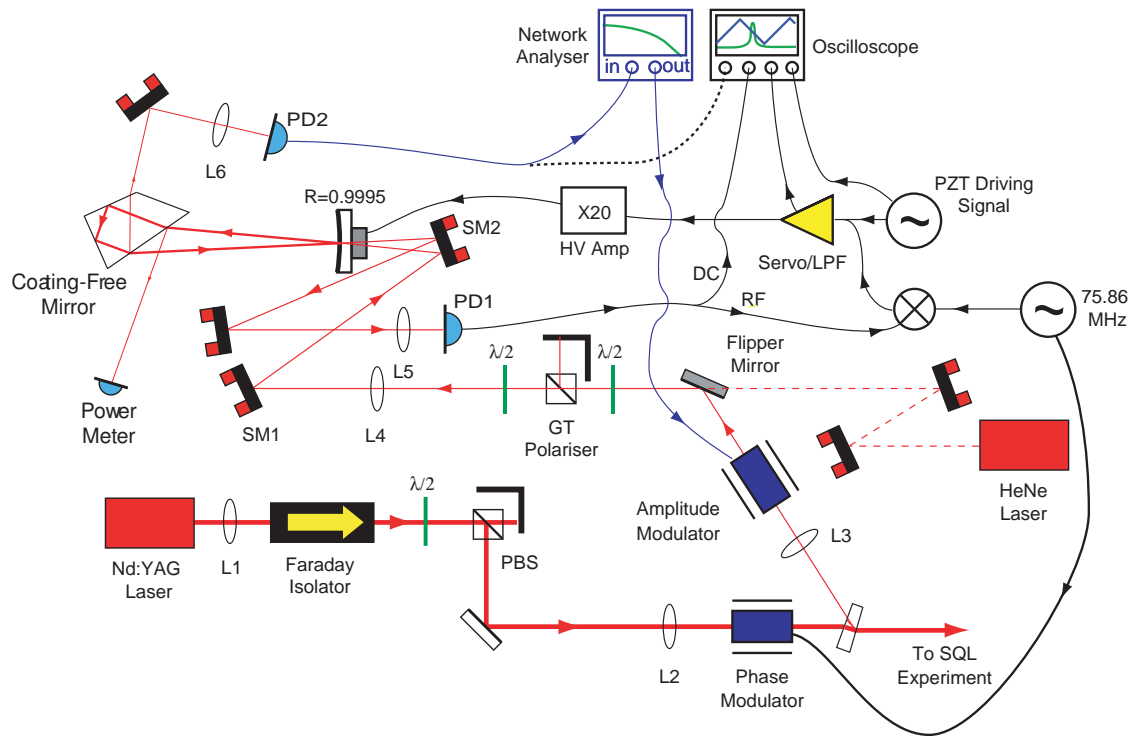
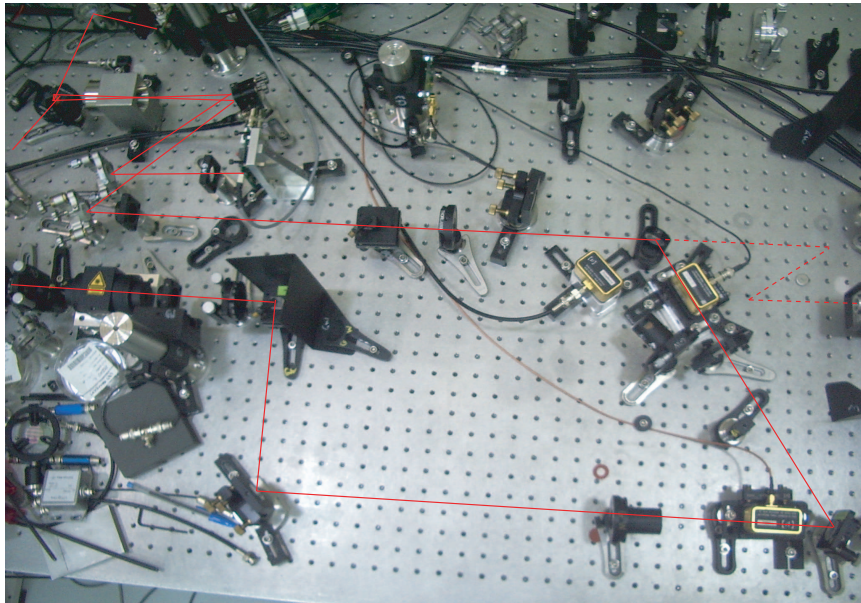


Figure 4.1.: A photograph of the optical components (top) in the experiment, taken from the same perspective as the Schematic of the experimental setup (bottom), which includes the electronics used for control of the cavity length. Some of the electronics are displayed in a different colour in order to differentiate those used for control of the cavity from those used for AM-sideband cavity interrogation.

mirrors provided the means to align the input beam to the fundamental eigenmode of the cavity, which was a two-mirror cavity comprised of the CFM and a conventional spherical mirror of reflectivity 99.95%. Photodetectors monitor the light leaving the cavity from two different points. PD1 monitors the reflected power, and was implemented as the cavity monitor for the control system, while PD2 aids in both cavity alignment and interrogation; the latter by its addition to the network analyser closed loop. The power meter measures the power of the fraction of the beam promptly reflected from the front face of the CFM.

The radio frequency (RF) signal from PD1 is mixed with a local oscillator signal in order to derive the error signal for cavity stabilisation. The servo receives the error signal, filters it appropriately, and provides the required amount of gain in order to return the position of the spherical mirror to the point of cavity resonance.

4.2. Measured Mirror Geometry

Initially, an experiment was set up in order to characterise the angles γ and σ as introduced in the mirror design chapter (Chapter 3). The necessity of knowing the exact angles is obvious from Equation 3.18. The values in this equation are substituted by those obtained from the measurements to create an appropriate theoretical model. Also the length of the cavity is derived from Equation 3.8 using the angle of the rear corner. This was required for mode-matching of the cavity.

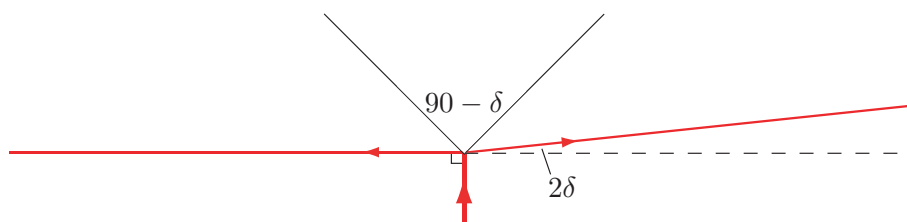


Figure 4.2.: Measurement of the CFM angles. In order to determine the angle of the rear corner, a laser was directed towards it such that it was divided into two reflected beams. From the relative angle of the beams, and value for the corner angle can be derived.

Figure 4.2 shows the measurement technique employed in the characterisation of the corner angle. A HeNe laser was set up such that the beam was aligned to a reference line on the table. The CFM was placed in the path of the beam such that the rear corner split the beam in two. By aligning the CFM such that left-hand reflected beam formed a right angle with the incident beam, the angle between the right-hand beam and the plane perpendicular to the input beam is 2δ . The position of the beam of interest was measured by using a razor edge, and the distance at which this was measured was maximised. The uncertainty of the positions of the beams corresponded to $\pm 0.05^\circ$ in the CFM corner angle. The same process was undertaken in working out the angle γ ; the angle the front face makes with the side of the corner reflector. This process was repeated for six different CFMs; five of which had an angle σ greater than 90° , despite being specified according

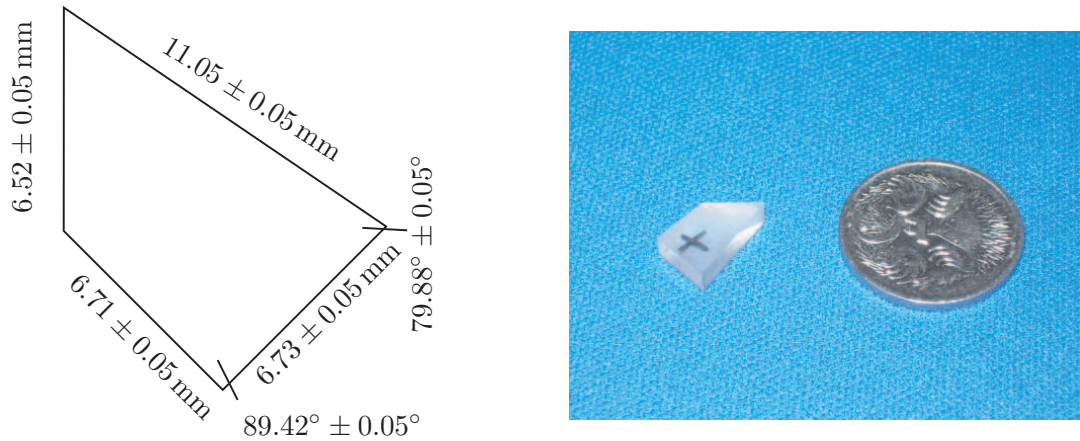


Figure 4.3.: The CFM dimensions, as measured in this experiment (left), and a photo of the CFM (right).

to the design in Chapter 3, and were unsuitable for the creation of a stable cavity with the conventional mirror.

Measurements of the spatial CFM dimensions were taken using a vernier caliper. Figure 4.3 shows these results, with associated uncertainties. The two TIR sides, along with the front face, were polished with an rms surface roughness of 0.5 nm, as specified by the manufacturer. Based on the measured dimensions, and the density of fused silica, $\rho = 2.65 \text{ g/cm}^3$, the weight of the CFM was calculated at 0.43 g, fulfilling the requirement that the optic weigh less than 0.5 g. The recorded dimensions are shown in Figure 4.3. The rear angle of $89.42^\circ \pm 0.05^\circ$ corresponded to a cavity length of approximately 7 cm.

4.3. Modematching

Before the cavity could be installed, the interrogating laser beam had to be matched to the cavity's fundamental eigenmode. The eigenmode was worked out using ABCD matrices as discussed in Section 2.3, using the mirror matrices provided in Appendix A. This calculation was performed for 1000 points in a two-mirror cavity, 7 cm in length, with a flat mirror and a mirror with radius of curvature $R = 0.5 \text{ m}$. These data are plotted in Figure 4.4, which shows the width and radius of curvature of the beam at each of these points. The cavity length was derived from the theoretical beam trajectories. This is determined, in particular, by the angle of the rear corner of the CFM. As in a two-mirror cavity, the length is defined as half the round-trip distance of the cavity. With knowledge of the cavity spatial mode, the beam could be matched to these parameters. The waist of the beam near the phase modulator was then characterised by performing measurements of the beam width using a beam profiler, or 'beamscan'. This device measures the size of the beam in the horizontal and vertical axes at successive points, separated by known distances, using these values to infer the waist size and its relative position. The phase modulator was used as the zero reference in the position measurements undertaken during the modematching procedure. The horizontal waist was found to have a radius of $280 \mu\text{m}$,

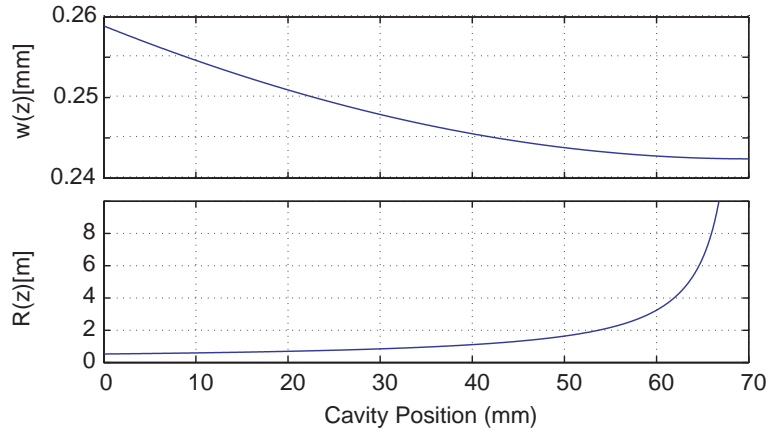


Figure 4.4.: The calculated beam width (top) and radius of curvature (bottom) of the fundamental cavity eigenmode for the 7 cm cavity, comprised of the CFM and a spherical mirror with a radius of curvature of 0.5 m.

located at 133 mm, and a waist radius of 256 μm , located at 108 mm, was observed for the vertical dimension. From this information, modematching¹ calculations could be done. One of the lenses used (L3) had a focal length of 200 mm, and the other (L4) had a focal length of 300 mm. Given the size and position of the beam waist near the phase modulator, the position at which these lenses should be placed was able to be determined. This was then tested by performing a beamscan at the position where the cavity was to be installed, in order to examine whether the beam would match the cavity eigenmode. Initially, the beam profile was almost correct, so small, empirical adjustments of the lens positions were performed, each time scanning the beam profile in order to approach the modematching criteria. Astigmatism in the beam could be compensated for by tilting

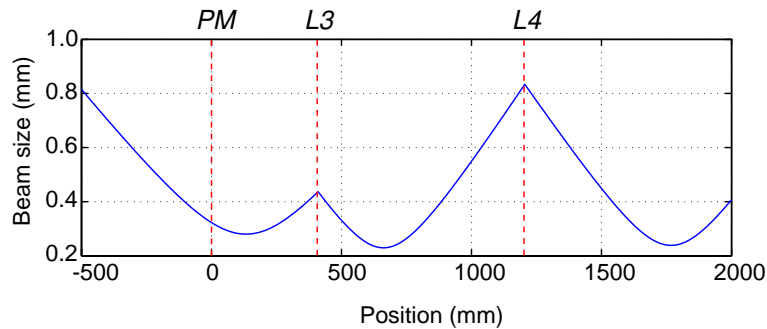


Figure 4.5.: The beam profile for the horizontal component of the beam plotted while performing the modematching calculations. The phase modulator was used as the zero reference point. The first waist of the beam is situated 133 mm past the PM and the waist size is 280 μm . L3 is situated at 410 mm, L4 at 1205 mm. The spherical mirror for the cavity is to be situated at 1700 mm.

¹Modematching was performed using the Beam Profiler program, by Alexei Ourjountsev, Ecole Normale Supérieure, Paris.

the lenses slightly. The required waist size corresponding to the cavity mode was $240\ \mu\text{m}$ at $1770\ \text{mm}$. The horizontal waist size was adjusted until it was $243\ \mu\text{m}$ at $1769\ \text{mm}$, and the vertical waist size was $231\ \mu\text{m}$ at $1841\ \text{mm}$. Here, L3 was situated at $410\ \text{mm}$ and L4 was situated at $1205\ \text{mm}$. Figure 4.5 shows the beam profile for this configuration.

4.4. Cavity Alignment

The CFM was mounted on a platform that was adjustable in the pitch and yaw degrees of freedom, shown in Figure 4.6. Adjustment of the yaw (referred to in this thesis as rotation of the CFM) of the platform was centered around a marker in the middle. When the CFM was mounted, the position at which the beam should enter the CFM was placed over this marker, in order that the CFM rotate around this point. The stand has two knobs in order to control the respective degrees of freedom. The pitch degree of freedom is not of interest in the CFM characterisation, as it will simply cause cavity resonance to break down in much the same way as tilting a flat mirror at this position would. The yaw degree of freedom is to be examined in this experiment, particularly as there is no way of determining if this degree of freedom is initially at the optimum operating point, and also to examine the characteristics of the CFM as it is rotated. Once the CFM was mounted, construction of the cavity could commence.

The cavity installation was performed by first positioning the CFM an adequate distance downstream of the steering mirrors (SM1 and SM2) in order allow enough room for the eventual installation of the spherical mirror, mounted to the PZT reaction mass. The pitch degree of freedom of the CFM mount was adjusted until the height of the beam reflected from the CFM was equal to the incident beam. Once this was done, the height of the platform was adjusted until the vertical position of beam incident on the CFM was observed to be halfway in between the top and bottom edges of the front face. The

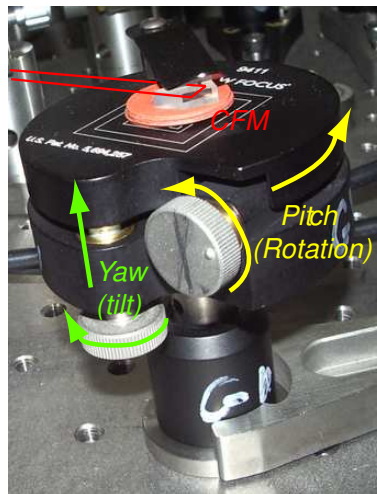


Figure 4.6.: The rotatable stand used to hold the CFM. The knob used to rotate the platform has a reference line (thicker line) to prevent the error in rotation from accumulating.

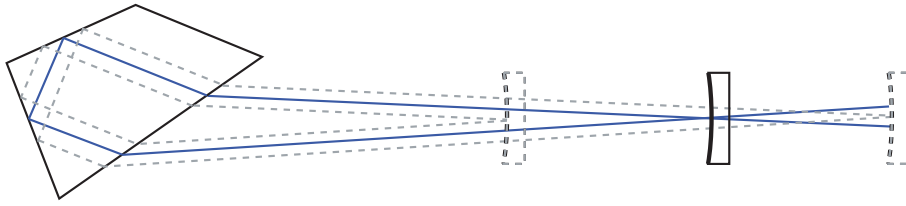


Figure 4.7.: Incorrect longitudinal placement of the spherical mirror does not prevent the cavity from resonating; the input beam can be adjusted to correct for this. However, as the spherical mirror is moved further from the ideal point, the beam within the CFM is more likely to suffer from diffraction effects, though the mirror design allows for some alignment freedom in this regime.

expected cavity length was approximately 7 cm, and as such the horizontal position of the platform was adjusted until the beams crossed at the appropriate point. This was the extent to which the CFM alignment could be determined before the spherical mirror was added to the cavity. Next, the beam reflected from the CFM was reflected back towards a photodetector, as shown in Figure 4.1. Two pinhole apertures were placed in the path of the reflected beam, to ensure the beam reflected from the spherical mirror follow the same path.

The spherical mirror was then clamped to the PZT, which was incorporated onto a heavy reaction mass. The spherical mirror was then placed at the observed point at which the input beam crosses with the output beam, as shown in Figure 4.7. Alignment was achieved by directing the beam back through the apertures. Referring to Figure 4.7, a slightly incorrect longitudinal positioning of the spherical mirror simply requires a transverse shift of the input beam using the steering mirrors.

Due to the low transmissivity of the spherical mirror at 1064 nm, a visible 633 nm HeNe laser was aligned to the input YAG beam using pinhole apertures, to help determine where the beam was within the cavity. At this wavelength the spherical mirror has a high transmissivity. A flipper mirror was raised or lowered depending on which beam was desired. This aided in adjusting the rotation, and also in determining the position of the beam reflected from the front face such that PD2 could be installed. This was not possible before the implementation of the control system, as cavity scans only cause the cavity to resonate for a short time, and the highly attenuated IR beam was not observable using an IR sensitive card in this regime.

Once this mirror was in place, the PZT was driven in order to scan the cavity length to observe if any light was resonant at this stage. Some small resonance peaks were observed, and this starting point allowed alignment of the cavity by walking the beam with the steering mirrors until only the TEM_{00} mode resonated in the cavity.

4.5. Cavity Scan

Once the alignment of the cavity was completed, an initial scan of the cavity was undertaken by driving the HV amplifier/PZT system with a sawtooth signal of $5V_{pp}$, at a frequency of 100 Hz; enough to scan the cavity over one FSR.

It was necessary to scan the cavity below a certain speed, due to the finite time it takes of the resonating power to reach a steady state. When the PZT was driven by the $5V_{pp}$, 100 Hz signal, many resonance lines were observed, each of a random magnitude, and subsequent scans showed no correlation in the heights or positions of these peaks.

Two effects were conspiring to provide these observations. Firstly, resonances within the mirror mounts respond to environmental perturbations, introducing cavity length changes that modulate the circulating field in an unknown fashion. This occurs due to noise alteration of the cavity length, randomly advancing or retarding the scan position as the length is swept over resonance. Secondly, as the cavity length is changed in order to probe the cavity frequency response, it is required that the length change is not too fast to allow the cavity to resonate. The environmental noise was reduced by switching off the air handling system in the laboratory, and taking the measurements at night.

The characteristic lifetime of the resonator was calculated in order to determine the amount of time over which the cavity should reach a steady state

$$\tau_p = \frac{1}{2\pi\text{FWHM}} \quad (4.1)$$

where τ_p is the time constant associated with the resonator. This was used in conjunction with a higher than expected finesse of 10,000 in order to place an upper bound on τ_p of approximately $1\ \mu\text{s}$. Thus, it was required that the PZT scan the cavity over resonance slowly enough to allow $1\ \mu\text{s}$ to pass. Calibration of the displacement of the PZT below resonance with respect to the input voltage was undertaken by noting that a scan through one Free Spectral Range corresponds to a spatial displacement of the driven mirror by $\lambda/2$. The voltage required to drive the PZT through a FSR was then recorded, giving a calibration of $2.24\ \mu\text{m}$ per Volt, defined by the voltage output of the signal generator, before amplification. Finally, the FWHM for a cavity with finesse 10,000, in terms of mirror detuning, is $53.2\ \text{pm}$. Thus it is required that the PZT scan over a distance of $53.2\ \text{pm}$ is a time greater than $1\ \mu\text{s}$ in order to ensure that the cavity has enough time to reach a steady state. This was done by reducing the frequency of the scan to 10 Hz, and the amplitude of the driving signal to less than $1.2V_{pp}$, according to the calibration provided.

4.5.1. FWHM and FSR

Subsequently, measurements of the FWHM and the FSR were taken in order to provide an initial characterisation of the CFM. This required the calibration of the oscilloscope timescale to the frequency detuning of the cavity. The modulation sidebands to be used for PDH locking were used for this calibration, as they appear at a known frequency offset with respect to the carrier.

Figure 4.8 displays the data recorded in this experiment. The data observed in Figure 4.8b provide the required calibration of the oscilloscope timescale to the known modulation frequency of 75.86 Mhz. This allowed a measurement of the FWHM from Figure 4.8a of $500 \pm 200\ \text{kHz}$. The large uncertainty is attributed to observed noise effects during data collection. In particular, acoustic noise caused a considerable change in the FWHM of the peak as subsequent scans were recorded. A FFT of the errorpoint was taken, which

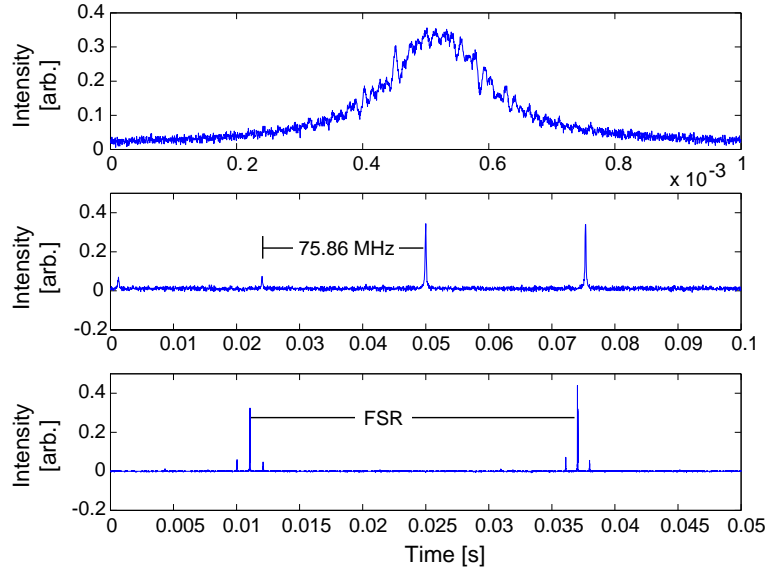


Figure 4.8.: (a) A close-up scan of the FWHM. (b) A scan of the cavity over resonance of the carrier and sidebands, executed at the same frequency and voltage as that in (a), for calibration of the FWHM. (c) a scan of the FSR of the cavity; the sidebands can be seen in this picture, enabling a calculation of the FSR. The peak heights appear different due to the high finesse of the cavity; the resolution of the oscilloscope was not adequate to give a true representation of the linewidth on this timescale.

was dominated by a large peak around 240 Hz. It is likely that this frequency corresponds to a resonance in the mirror mount coupling with acoustic noise.

Figure 4.8c provides a scan of the entire free spectral range of the cavity, along with the sideband reference. From this, the FSR was determined to be 2030 ± 50 MHz. Using this value with the previously calculated FWHM gives a finesse of $\mathcal{F} = 4060^{+2540}_{-1100}$. The large errors are due primarily to the large error obtained for the FWHM. Rearranging the equation for the finesse (Equation 2.22) to solve for r_2 , with $r_1 = \sqrt{0.9995}$

$$r_2 = \frac{1}{r_1} + \frac{\pi^2}{2\mathcal{F}^2 r_1} - \frac{\pi\sqrt{4\mathcal{F}^2 + \pi^2}}{2\mathcal{F}^2 r_1} \quad (4.2)$$

a CFM reflectivity of $99.90^{+0.05}_{-0.06}\%$ was obtained.

4.5.2. Beam Transverse Alignment

Substitution of the experimentally derived value, $\delta = 0.58 \pm 0.05^\circ$, into Equation 3.8, gives the length L between the front face of the CFM and the spherical mirror, followed by the addition of the beam optical path of approximately 15 mm within the CFM, provided a predicted round trip cavity length of

$$L_{RT} = 2L + 15 \text{ mm} = 130 \pm 11 \text{ mm} \quad (4.3)$$

where L_{RT} is the round trip cavity length. The cavity length can also be derived from the FSR, corresponding to a cavity length of 147 ± 5 mm, falling just outside the uncertainty of Equation 4.3. Equation 4.3 assumes the beam is incident on the Brewster window at the ideal point. The FSR derived cavity length suggests that the beam is incident at a point which is at most 0.4 mm closer to the vertical edge of the Brewster window than this. This was derived by calculating the effective length change of the cavity as one moves the input beam horizontal position.

The exact vertical position of the beam incident on the front face could not be determined, as there was no experimental information to provide a means for constraining this variable other than a direct observation of the beam during the cavity setup.

4.6. Control System

In order to obtain the CFM reflectivity to a higher accuracy, an observation of the cavity frequency response to an amplitude modulated carrier was required to be taken while the cavity was locked. The PDH laser frequency stabilisation technique was used to hold the cavity on resonance, as described in Section 2.5.2. In this case, contrary to the regime suggested in the name, the cavity length was stabilised; an equivalent way to maintain the desired relationship between the laser frequency and the cavity length. In order to implement this control system, an Agilent 33250A signal generator was used to generate a 75.86 MHz signal input into the phase modulator. The phase modulator was a New Focus 4003 Resonant IR phase modulator specified at 75 MHz, and a resonant photodetector at 75 MHz was used for detection. The servo control board was manufactured in-house, as was the high voltage amplifier, and the mixer used to obtain the DC control signal was a Mini-Circuits ZAY-3 specified over 0.07 - 200 MHz. The control system was assembled as shown in Figure 4.1.

4.6.1. Servo and PZT Frequency Response

In order to ensure that the control system was stable, the servo must take into account large phase delays in the system, such as that at the resonance of the PZT. This is done with the use of an elliptic filter incorporated in the servo board, which provides large attenuation at the frequency of the PZT resonance. Since the PZT resonance frequency is different for individual PZTs, a measurement of the frequency response of the PZT was necessary to enable correct servo design.

The response of the PZT was obtained by placing it in a Michelson interferometer. By driving the PZT with a small signal generated by the network analyser, its frequency response was obtained by detection of the Michelson interferometer transmitted beam. The change in power of the transmitted Michelson interferometer beam was maximised by holding the relative arm lengths at the point at which 50% of the incident power is transmitted through the antisymmetric port. This is also the point where the response is essentially linear for small driving signals. The Michelson interferometer was maintained at this point by monitoring the transmitted power, and adjusting the DC mirror position with the servo DC offset.

Figure 4.10 shows the measured frequency response of the PZT. A large resonance in the PZT response is observed around 33 kHz, with many smaller peaks appearing at higher frequencies.

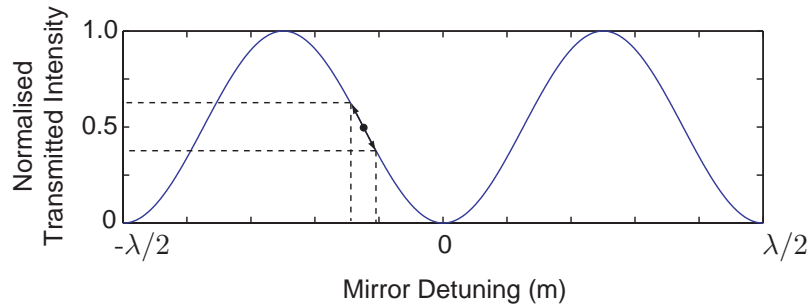


Figure 4.9.: Response of the Michelson interferometer used to obtain the PZT frequency response. As the mirror is driven with a swept sinusoid, the michelson transmitted intensity responds linearly, provided the signal driving the PZT is not too large. The Michelson was held at this point by using the DC control of the servo.

In order to obtain the open loop frequency response of the control servo, a network analyser was used with a swept sinusoid output driving the servo circuit with a voltage of 10 mV. The response was taken from the servo output, and displayed on the network analyser. The obtained response is plotted in Figure 4.10, where the servo response shows maximum attenuation at 31 kHz, close to the resonance frequency of the PZT.

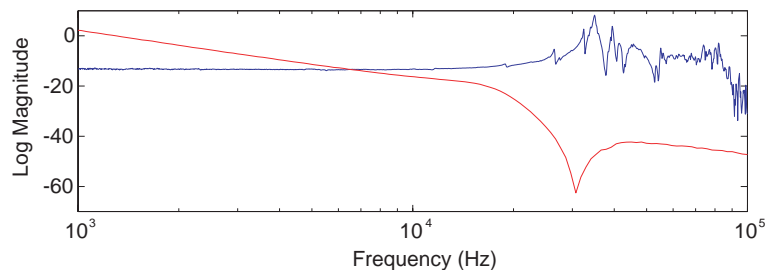


Figure 4.10.: Open loop frequency response of the PZT (blue) and the servo (red). The PZT resonance is attenuated by an elliptic filter incorporated into the servo board.

4.6.2. Locking the Cavity

Once the control system was set up, the error-signal monitor output on the servo was used to observe the error signal on the oscilloscope. The relative phase of the RF signal from the photodiode and the LO signal was adjusted by changing the cable length in order to optimise the demodulation phase, and therefore, the error signal. Figure 4.11 shows its final form.

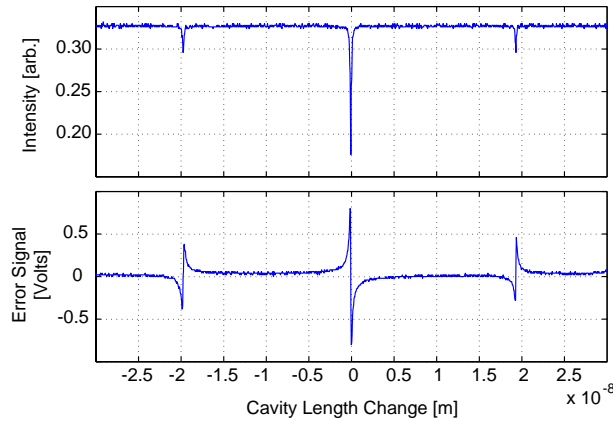


Figure 4.11.: The voltage from PD1 at DC as the cavity is scanned (top) and the error signal (bottom). The sidebands have small error signals of their own, and the control system can lock to these when the polarity of the PZT driving signal is incorrect. Notice that the scanning the cavity decomposes the input light into its spectral components. In this way a two mirror cavity can be used as a spectrum analyser.

To lock the cavity, the DC offset of the servo was varied until the cavity length passed over the point of resonance. The servo gain was then turned on, and the cavity acquired lock. This was observed by a drop in the reflected power detected by PD1. The gain was then adjusted until the noise in the locked error-signal was minimised. The servo was able to maintain lock indefinitely in the absence of extra atmospheric noise.

4.7. CFM Reflectivity

Cavity locking enabled the reflectivity to be determined with a greater accuracy by mapping out the frequency response with the use of amplitude modulated sidebands.

4.7.1. AM-Sideband Cavity Interrogation

Before the frequency response of the cavity could be recorded using this technique, calibration of the network analyser was required. By detecting the beam with the photodetector before it is incident on the cavity, the network analyser is able to record the frequency dependence of the peripheral components of the system, which can then be corrected for in order that only information about the system of interest, in this case the CFM cavity, can be extracted.

Once this calibration was made, the cavity was locked. By maintaining the cavity at resonance, the amplitude modulated sidebands interrogate the response of the cavity around this position. As the frequency of the AM sidebands was increased, information about the frequency dependence of the cavity was modulated onto them, in terms of both transmitted power and phase. The photodetector was then positioned such that Beam 2 be incident upon in. From the measured response, the frequency at which the magnitude is 3 dB, or the phase is 45°, less than that measured at the cavity resonance

frequency is the half width at half maximum (HWHM) of the cavity. These results allow a direct derivation of the mirror reflectivity using a least squares fitting method², with the reflectivity as the fitted variable. A series of such data were taken; the mirror rotated incrementally between each.

4.7.2. CFM Reflectivity

The zero point for CFM rotation was defined as the rotational position where the powers from the two beams reflected from the CFM front face (Beam 1 and Beam 2) were equal in power. From the data recorded using the AM method, the reflectivity of the CFM under ideal rotational alignment was determined to be 0.9989 ± 0.0001 at a CFM rotation $\rho = 0.23^\circ \pm 0.025^\circ$. The FWHM of the cavity was 560 kHz. These data correspond to a cavity finesse of 3930 ± 260 . Possible factors that may cause the reflectivity of the CFM to deviate from the theoretically predicated value of 0.9997 are (1) the possibility that the vertical position at which the beam enters the CFM was not ideal, which can cause part of the beam power to be clipped by the edges of the front face, and (2) scatter due to surface roughness of the TIR surfaces.

Figure 4.12 shows the data obtained, using AM-sideband cavity interrogation, for the CFM rotation corresponding to the maximum observed reflectivity.

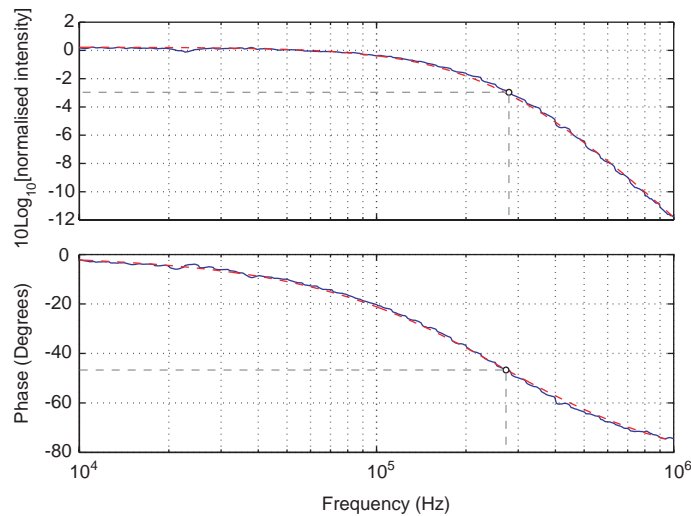


Figure 4.12.: The measured frequency (top) and phase (bottom) response of the cavity for the rotation of the CFM ($\rho = 0.23^\circ \pm 0.025^\circ$), at which the maximum CFM reflectivity was observed. The blue curve shows the experimental data, while the red dashed line shows the least squares fit used to determine the reflectivity. The -3dB point, corresponding to the HWHM of the frequency response curve is marked, along with the equivalent 45° phase point. The linewidth measured for this case was 560 kHz, and the least squares fit yielded a CFM reflectivity of 0.9989 ± 0.0001 .

²This was achieved using the curve-fitting tool in the Matlab Toolbox, along with a custom equation based on Equation 2.10.

4.7.3. CFM Rotation Calibration

The reflectivity of the CFM depends on its rotational alignment, as the incident and out-coupled beam passing through the front face of the CFM deviate from optimum Brewster angle coupling when misaligned. In order to find the optimal rotational alignment of the CFM, and to map out its reflectivity as a function of angle, its rotational alignment was incrementally changed. At each of these rotational steps its reflectivity was derived via the AM cavity interrogation method described above. To obtain the reflectivity of the CFM as a function of its rotational angle, the rotation actuator on the CFM stand requires calibration.

In order to calibrate the rotation of the CFM, the precision adjustment screw was calibrated to the rotation of the platform itself, in terms of rotation angle per turns of the screw. To do this, the change in angle of Beam 1 was observed, as the knob was rotated through one full turn. The error was minimised by maximising the distance from the CFM at which it was measured. The beam measurement was taken by using an upright metal block with a ruler drawn onto it with markings at 2 mm intervals. The block was positioned such that half the beam profile was incident at the edge. The platform rotation screw was then turned, and the transverse distance moved by the beam was recorded after one full turn. Because the CFM is mounted such that rotation is around the point at which Beam 1 reflects from the front face, the CFM rotation is half the change in the angle of this beam. The mounting platform rotation was calibrated by this method to be $0.9^\circ \pm 0.1^\circ$ for each full turn of the adjustment screw.

For each measurement, the knob seen on the CFM stand in Figure 4.6 is rotated by 1/8 of a turn. Clockwise turns of the knob correspond to clockwise rotations of the CFM platform, and are represented as negative rotations in the data. Anti-clockwise turns corresponds to anti-clockwise rotations of the CFM platform and arise as positive rotations in the data. Twelve data points were taken for both the positive and the negative rotational directions. The error in the amount by which the adjustment screw is turned is not cumulative, as the rotation was measured by a reference line on the head of the adjustment screw (see Figure 4.6). The uncertainty in the adjustment screw angle for each rotational increment was judged to be $\pm 5^\circ$. Thus, the magnitude of the CFM rotation between each measurement is $0.113^\circ \pm 0.025^\circ$. For each recorded datum, this uncertainty was translated to an uncertainty in the measured value, and added to the vertical axis uncertainty.

4.7.4. Reflectivity Vs. Rotation

As the CFM is rotated, it exhibits a change in reflectivity due to the angular dependence of the front face transmission. These data were recorded by measuring the cavity response, using the amplitude modulation technique described above, for each iterative mirror rotation. The theoretical curve was fitted to the data by adding extra loss of 0.08% in the CFM, corresponding to the difference between the maximum reflectivity observed and that predicted by the original model.

The data are presented in Figure 4.13, and agrees with the theory for clockwise rotation of the CFM. For anti-clockwise rotation, a deviation from the theory can be seen as a

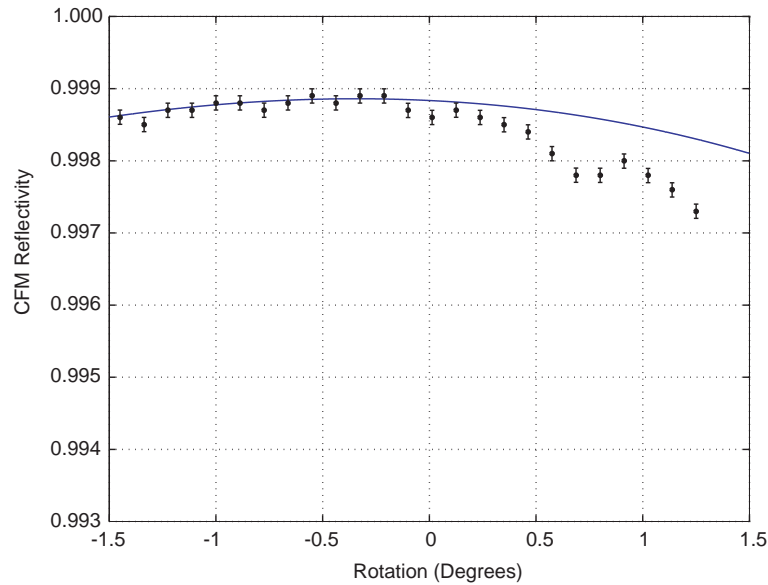


Figure 4.13.: Reflectivity of the coating-free mirror as a function of rotation. These data were taken from a least squares fit of the frequency and phase response of the cavity, obtained using swept amplitude modulation of the carrier while the cavity was on resonance. The theoretical curve was fitted to the data by increasing the loss in the CFM. The errors are given due the 95% confidence intervals, as calculated by the curve fitting software.

drop in the reflectivity of the mirror, caused by a phenomenon not included in the model. This is possibly due to clipping of the beam as it propagates through the CFM, either at the front face or at the reflective surfaces. The uncertainty in Figure 4.13 is due to the 95% confidence interval observed during the curve fitting procedure, and was roughly ± 0.0001 for each fit.

4.7.5. Non-Perfect Total Internal Reflection

The observed deviation of 0.08% in the reflectivity of the CFM, as compared to the theoretical prediction, can be added to the CFM cavity equations by setting $r_{TIR}^2 = 0.9996$. This attributes all of the cavity loss to scattering at the TIR reflector surfaces, thus placing an upper bound on the magnitude of this effect of 0.04% per reflection. Referring to Figure 4.14, there was strong evidence of scattered light inside the CFM from these surfaces. A numerical investigation of TIR scattering due to random surface roughness is undertaken in [Nieto '92], though none of the cases investigated therein provide numerical values for a surface roughness corresponding to that of the polished CFM surfaces. Surface roughness was also attributed as the main source of loss in a fused silica monolithic TIR resonator [Schiller'92]. It is possible to reduce the effects of this phenomenon dramatically by super-polishing the reflective surfaces to rms values in the sub-Angstrom regime, where TIR reflects 99.9999% of the power [Brown '86, Hudgens '98].

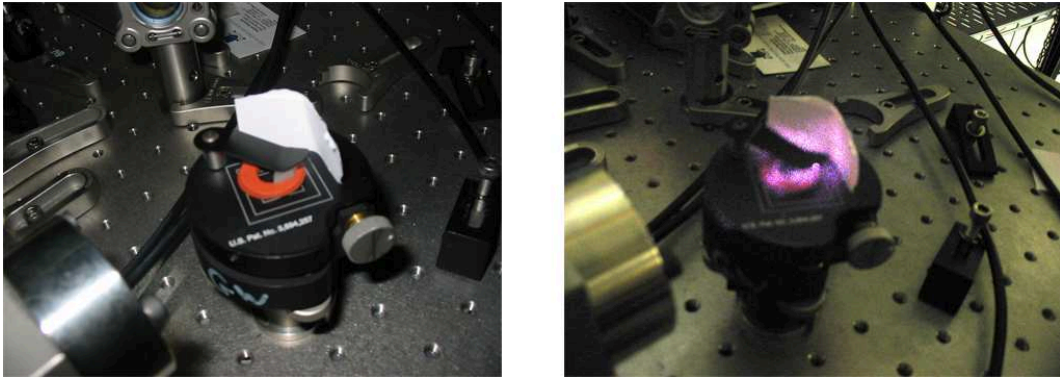


Figure 4.14.: The CFM while the cavity is non-resonant (left). When the cavity resonates, there is strong evidence to suggest that scattering occurs at the CFM reflective surfaces in the form of light exiting the cavity at these locations. The piece of paper was added for observation of the scattered light.

4.8. Intracavity Power

For a fixed input beam alignment, the sensitivity of the two-mirror cavity to CFM misalignment was investigated by an indirect observation of the intracavity power. As the CFM is rotated, the point at which the input and output beams converge is no longer at the surface of the conventional mirror, as shown in Figure 4.15. This results in the respective beam positions being slightly offset at this point, and part of the circulating power does not reproduce as desired. It is evident that this effect causes a reduction in circulating power as the CFM is rotated, in addition to that due to the change in CFM reflectivity.

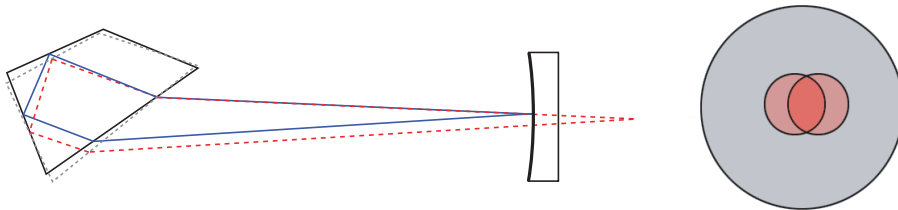


Figure 4.15.: The effect of mirror rotation on the position where the beams converge (left - not to scale). For a fixed input mirror, this translates to a reduction in the portion of the beam that is self-reproductive (right - not to scale).

This was able to be investigated qualitatively by probing the resonant intracavity power with measurements of the beam reflected from the front face of the CFM (Beam 1). This beam gives an indication of the cavity power for a given rotation, weighted by the rotationally dependent reflectivity of the front face. This is compared to the calculation of the power Beam 1 would have, if the change in reflectivity of the Brewster window would be solely responsible for changes in intracavity power. As such, the difference between

this calculated curve and the measured power represent power lost due to misalignment. Figure 4.16 plots the data obtained for the beam power. Equation 3.20 was used to plot the theoretical curve. From this, it is clear that circulating power is lost from the TEM_{00} mode as the CFM is rotated.

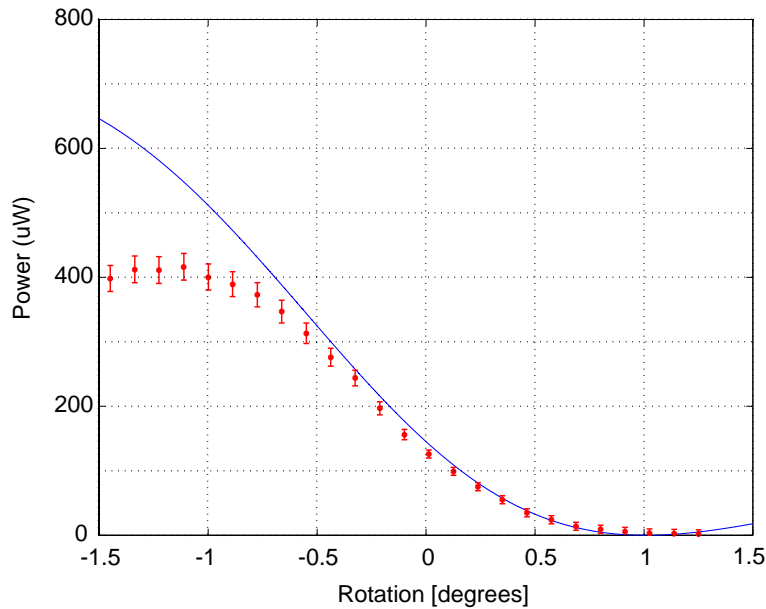


Figure 4.16.: The power reflected from the front face of the CFM as a function of rotation. The solid line is derived under the assumption that no cavity mismatch occurs, and changes in intracavity power are caused only by deviations of the beams from the Brewster angle at the CFM front face. Thus, the difference between this curve and the experimental values corresponds to the power lost from the TEM_{00} mode.

4.9. Transverse Electric Polarisation

For completeness, a scan of the cavity for the TE polarisation is included. The FWHM is much wider than that observed for the TM polarisation, at 82 ± 5 MHz, as expected due to the high reflectivity of the brewster windows in this regime. This corresponds to a finesse of 25 ± 2 . These results were derived by direct observation of the data, and the uncertainties are due to the noise at both the maxima and minima of the data. This finesse corresponds to a CFM reflectivity of $77.8 \pm 2.1\%$. This verifies the necessity for the use of TM polarisation if a highly reflective CFM is desired.

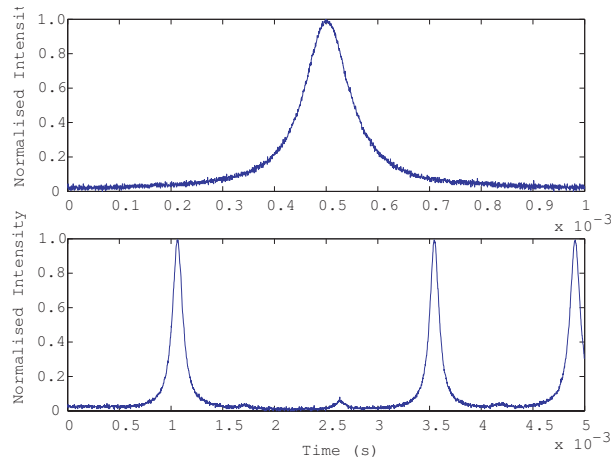


Figure 4.17.: A close-up scan of the frequency response of the cavity for the TE polarisation (top), and a scan of the FSR for the same polarisation (bottom).

4.10. Summary

The CFM was included as one of the optics in a two-mirror cavity, along with a conventional mirror of 99.95% reflectivity. This cavity was stabilised to the laser frequency with the use of PDH locking. This allowed a detailed interrogation of the frequency response of the cavity using an AM sidebands modulation technique, from which the reflectivity of the CFM could be determined. Investigations of the CFM reflectivity as a function of rotational alignment angle showed good agreement with the theoretical model, which was fitted to the experimental data by including a loss of 0.04% due to scatter at the TIR surfaces. Qualitative investigations of the cavity power suggest that the CFM cavity is insensitive to misalignment, when compared to a conventional optic.

For the optimum rotational alignment a reflectivity of 99.89% was observed for the CFM, corresponding to a cavity finesse of approximately 4000.

Chapter 5.

Summary and Future Work

5.1. Summary

Highly sensitive interferometry will be limited by thermal noise in optical coatings. It is predicted that Advanced LIGO will be limited by coating thermal noise in its most sensitive frequency band. This discovery has stimulated investigations into the losses associated with optical coatings, and it is evident that noise associated with these losses will decrease the likelihood of a successful observation of the standard quantum limit.

The design and characterisation of a lightweight, highly reflective coating-free mirror has been presented as a means for eliminating this prohibitive source of noise. The use of reflective coatings was avoided by taking advantage of the phenomenon of total internal reflection, inside a substrate of highly transmissive fused silica. The light was coupled into and out of the substrate via Brewster's angle, necessitating the use of transverse magnetic polarised light. The weight of the CFM was calculated to be 0.43 g, well within the goal of less than 0.5 g.

The reflectivity of the CFM was characterised by its inclusion in a two-mirror cavity. The other optic of the cavity was a highly reflective, conventional spherical mirror of high quality. A resonant cavity was successfully built from these two mirrors, and the cavity was stabilised to the laser frequency with the use of PDH locking. This allowed to interrogate the frequency dependence of the cavity response, with the use of AM modulated sidebands. From this interrogation of the cavity the reflectivity of the CFM could be determined. Also the power of the beams reflected from the front face of the CFM was monitored to obtain information about the intra-cavity power. Due to the dependence of the CFM reflectivity of the rotational alignment, collection of these data for many CFM rotational alignment positions was undertaken.

The data was compared to a theoretical model that plotted the expected CFM reflectivity as it was rotated. The theoretical model was fitted to the data by the addition of loss at the surfaces of total internal reflection, which were specified to have a surface roughness of 0.5 nm rms. This placed an upper bound of the loss at each of these surfaces of 0.04%. The maximum finesse of the cavity was determined to be about 4000, corresponding to a reflectivity of the CFM 99.89%. In conclusion, the objective of creating a lightweight highly reflective coating-free mirror was well achieved. However, with a few alterations, the reflectivity of such a CFM can be further improved as is discussed in the following section.

5.2. Future Work

The loss due to scattering at the TIR surfaces can be reduced by reducing the surface roughness via superpolishing [Brown '86]. This can provide a reflectivity of 99.9999% from these surfaces [Hudgens '98]. The loss of the beams in- and outcoupled of the CFM can be reduced by altering the front face of the CFM such that both beams are incident without deviating from Brewster angle. By combining these two improvements, the CFM promises to be limited by internal transmission loss only.

Although no photothermal effects were observed in the CFM this can become problematic when operating it with higher input powers. If need arises, a CFM can be made from Suprasil SV311 grade fused silica, which has an absorption of only 0.2 ppm/cm, more than one order of magnitude less than Suprasil 1 as used for the CFM described in this thesis. The same consideration applies for thermal lensing inside the CFM.

An all coating-free cavity consisting of two CFMs as described in this thesis would be a plane-plane cavity, and hence difficult to handle. This can be accounted for by putting a curvature to one of the TIR faces of one of the CFMs. However, as this would introduce astigmatism, a corrective cylindrical curvature has to be overlaid to the curved surface. Another, more complex, method to create a stable cavity with two CFMs is to utilise thermal lensing inside the substrates. This necessitates the use of high optical power or a substrate material with stronger absorption. As the cold cavity would not be stable, an auxiliary laser could be used to write the thermal lens into the substrate prior to operating the cavity.

Extending this to creating a Michelson interferometer can be done according to Figure 5.1. This includes the implementation of a coating-free beamsplitter. Such a beamsplitter can be realised using evanescent coupling, or frustrated total internal reflection. Principally, a coating-free Michelson interferometer can incorporate power- and signal-recycling mirrors as well as arm cavities. Evanescent coupling requires precise position control of the relevant optical components but on the other hand allows to dial the reflectivity in.

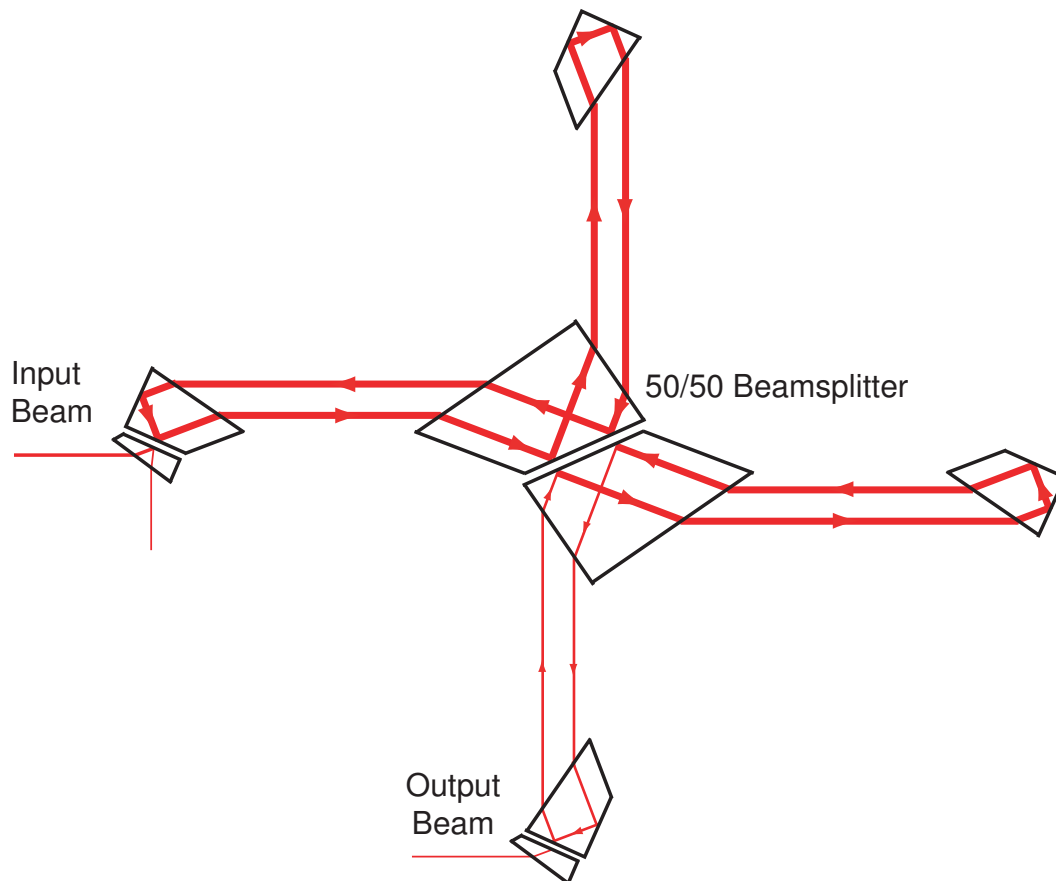


Figure 5.1.: A design of an all coating free dual-recycled Michelson interferometer. The beam-splitter as well as the power- and signal-recycling mirror are based on evanescent coupling. The design can be further advanced by implementing arm cavities. The input mirrors for the arm cavities would also need to be based on evanescent coupling. An advantage of evanescent coupling is the fact that the reflectivity of the optic can be dialled in.

Appendix A.

ABCD Matrices

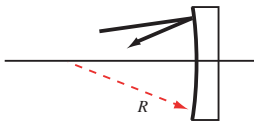
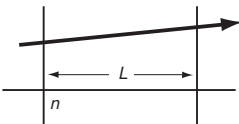
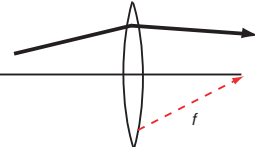
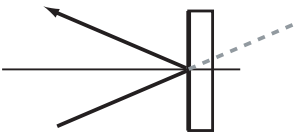
 <p>Reflection from a spherical mirror with radius of curvature R</p>	$\begin{pmatrix} 1 & 0 \\ -2/R & 1 \end{pmatrix}$
 <p>Propagation of a distance L through a homogeneous medium of refractive index n</p>	$\begin{pmatrix} 1 & L/n \\ 0 & 1 \end{pmatrix}$
 <p>Transmission through a mirror of focal length f</p>	$\begin{pmatrix} 1 & 0 \\ -1/f & 1 \end{pmatrix}$
 <p>Reflection from a plane mirror</p>	$\begin{pmatrix} 1 & 0 \\ 0 & 1 \end{pmatrix}$

Figure A.1.: Optical components (left) and their corresponding ABCD matrices (right)

Appendix B.

Tabulated Experimental Data

Turns	\mathcal{F}	$R_{CFM}(\%)$	$P_{B1}(\mu\text{W})$
1 1/2	1960 ± 60	99.73 ± 0.01	1.96
1 3/8	2160 ± 80	99.76 ± 0.01	2.3
1 1/4	2320 ± 90	99.78 ± 0.01	3.4
1 1/8	2510 ± 100	99.80 ± 0.01	5.5
1	2320 ± 90	99.78 ± 0.01	9.1
7/8	2320 ± 90	99.78 ± 0.01	14
3/4	2620 ± 110	99.81 ± 0.01	24
5/8	2990 ± 150	99.84 ± 0.01	35
1/2	3140 ± 160	99.85 ± 0.01	55
3/8	3310 ± 180	99.86 ± 0.01	75
1/4	3490 ± 200	99.87 ± 0.01	99
1/8	3310 ± 180	99.86 ± 0.01	126
0	3490 ± 200	99.87 ± 0.01	156
-1/8	3930 ± 260	99.89 ± 0.01	197
-1/4	3930 ± 260	99.89 ± 0.01	244
-3/8	3690 ± 230	99.88 ± 0.01	276
-1/2	3930 ± 260	99.89 ± 0.01	313
-5/8	3690 ± 230	99.88 ± 0.01	347
-3/4	3490 ± 210	99.87 ± 0.01	373
-7/8	3690 ± 230	99.88 ± 0.01	389
-1	3690 ± 230	99.88 ± 0.01	400
-1 1/8	3490 ± 210	99.87 ± 0.01	416
-1 1/4	3490 ± 210	99.87 ± 0.01	411
-1 3/8	3140 ± 160	99.85 ± 0.01	412
-1 1/2	3310 ± 180	99.86 ± 0.01	398

Table B.1.: Data corresponding to Figure 4.13. The finesse of the cavity is calculated for each measured reflectivity, obtained from a least squares fit of the HWHM taken from the AM cavity interrogation technique. Also, the measured power of Beam 1 for the corresponding rotational positions is included. The values in bold correspond to the point of optimum alignment.

Appendix C.

The Relationship Between Finesse, FWHM, and FSR

Many experiments with optical resonators make use of the relationship between FWHM, FSR, finesse, and the reflectivity of the mirrors. In particular, the ability to express the finesse interchangeably as a function of observed experimental results in terms of FWHM and FSR, and as a function of a theoretical mirror reflectivity. We show that a derivation of the mirror reflectivity using this method is valid for almost all practical optical resonators.

Consider the cavity transmitted field given by the following equation,

$$\frac{E_{trans}}{E_{inc}} = \frac{i\sqrt{1 - \mathcal{S}^2}e^{i\psi}}{1 - \mathcal{S}e^{i\phi}} \quad (\text{C.1})$$

where \mathcal{S} is the single round trip transfer function given by the cavity parameters (ie. a Fabry-Perot Cavity has $\mathcal{S} = r_1 r_2$), ϕ is the round-trip phase shift of the cavity, and ψ is the phase shift from the cavity entrance to the point of transmission. The power of the transmitted field is given by,

$$\frac{P_{trans}}{P_{inc}} = \frac{1 - \mathcal{S}^2}{1 - 2\mathcal{S} \cos \phi + \mathcal{S}^2} \quad (\text{C.2})$$

with a free variable ϕ . We would like to find out the value for ϕ when the transmitted power is one half of that which the cavity gives out on resonance ($\phi = 0$),

$$\frac{P_{trans}}{P_{inc}} = \frac{1}{2} \frac{P_{trans}}{P_{inc}} \Big|_{\phi=0} \quad (\text{C.3})$$

with the appropriate substitutions, this becomes,

$$\frac{1 - \mathcal{S}^2}{1 - 2\mathcal{S} \cos \phi + \mathcal{S}^2} = \frac{1}{2} \left(\frac{1 - \mathcal{S}^2}{1 - 2\mathcal{S} + \mathcal{S}^2} \right) \quad (\text{C.4})$$

After some algebra, we get,

$$\cos \phi = \frac{2\mathcal{S} - (1 - \mathcal{S})^2}{2\mathcal{S}} \quad (\text{C.5})$$

Now, operating on both sides with the inverse cosine,

$$\phi = \arccos \left(\frac{2\mathcal{S} - (1 - \mathcal{S})^2}{2\mathcal{S}} \right) \quad (\text{C.6})$$

Referring to Figure C,

$$\phi = \arctan \left(\frac{x}{2\mathcal{S} - (1 - \mathcal{S})^2} \right) \quad (\text{C.7})$$

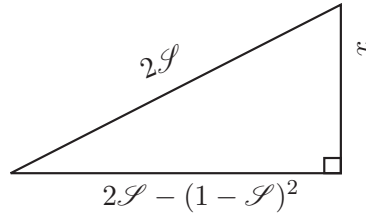


Figure C.1.: This triangle is used in order to re-express the arccos expression for ϕ in terms of arctan.

where,

$$x = (1 - \mathcal{S})\sqrt{4\mathcal{S} - (1 - \mathcal{S})^2} \quad (\text{C.8})$$

Therefore,

$$\phi = \arctan \left(\frac{(1 - \mathcal{S})\sqrt{4\mathcal{S} - (1 - \mathcal{S})^2}}{2\mathcal{S} - (1 - \mathcal{S})^2} \right) \quad (\text{C.9})$$

The right-hand side is small for $\mathcal{S} \rightarrow 1$, so we use the approximation, $\arctan x \simeq x$,

$$\phi \simeq \frac{(1 - \mathcal{S})\sqrt{4\mathcal{S} - (1 - \mathcal{S})^2}}{2\mathcal{S} - (1 - \mathcal{S})^2} \quad (\text{C.10})$$

After some more algebra, we have,

$$\phi \simeq \frac{2\sqrt{\mathcal{S}}(1-\mathcal{S})\sqrt{1+\frac{(1-\mathcal{S})^2}{4\mathcal{S}}}}{2\mathcal{S}-(1-\mathcal{S})^2} \quad (\text{C.11})$$

We are considering a cavity of high finesse ($\mathcal{S} \rightarrow 1$), and so the the following simplifications can be made to Equation C.11

$$\frac{(1-\mathcal{S})^2}{4\mathcal{S}} \rightarrow 0 \quad (\text{C.12})$$

$$(1-\mathcal{S})^2 \rightarrow 0 \quad (\text{C.13})$$

and equation C.11 simplifies to,

$$\phi \simeq \frac{(1-\mathcal{S})}{\sqrt{\mathcal{S}}} \quad (\text{C.14})$$

Finally, noting the following expansion for ϕ ,

$$\phi = kL \quad (\text{C.15})$$

$$k = \frac{2\pi}{\lambda} \quad (\text{C.16})$$

$$\lambda = \frac{c}{\nu} \quad (\text{C.17})$$

therefore,

$$\phi = \frac{2\pi\nu L}{c} \quad (\text{C.18})$$

and thus we end up with,

$$\phi = \pi \frac{FWHM}{FSR} \quad (\text{C.19})$$

where,

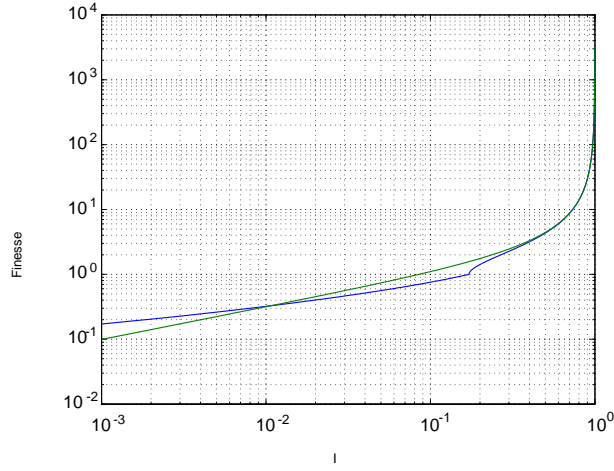


Figure C.2.: The blue line shows the exact representation of $\frac{FWHM}{FSR}$, and the green line shows the approximation we derived. For values of \mathcal{S} above about 0.5, the approximation is very close to the exact value.

$$2\nu = FWHM \tag{C.20}$$

from the conditions imposed by Equation (C.3), and,

$$\frac{c}{L} = FSR \tag{C.21}$$

Substituting back into Equation (C.14), and rearranging, we get,

$$\frac{FSR}{FWHM} \simeq \frac{\pi\sqrt{\mathcal{S}}}{1 - \mathcal{S}} \tag{C.22}$$

and setting $\mathcal{S} = r_1 r_2$, Equation (C.22) becomes,

$$\frac{FSR}{FWHM} \simeq \frac{\pi\sqrt{r_1 r_2}}{1 - r_1 r_2} \tag{C.23}$$

Thus, we have proven the relationship of the two equations which give the finesse. Figure C shows for what values of \mathcal{S} the approximations we have made will hold.

Bibliography

- [Albiol '92] F. Albiol, S. Navas, and M. V. Andres *Microwave experiments on electromagnetic evanescent waves and tunneling effect* Am. J. Phys. **61** 2 (1992) 165-169
- [Barr '02] B. W. Barr, G. Cagnoli, M. M. Casey, D. Clubley, D. R. M. Crooks, K. Danzmann, E. J. Ellifi, S. Goßler, A. Grant, H. Grote, A. Heptonstall, J. Hough, O. Jenrich, H. Lück, S. A. McIntosh, G. P. Newton, D. A. Palmer, M. V. Plissi, D. I. Robertson, N. A. Robertson, S. Rowan, K. D. Skeldon, P. Sneddon, K. A. Strain, C. I. Torrie, H. Ward, P. A. Willems, B. Willke, W. Winkler *Silica Research in Glasgow Class. Quantum Grav.* **19** (2002) 1655–1662
- [Black '00] E. Black *An Introduction to Pound-Drever-Hall Laser Frequency Stabilization* Am. J. Phys. **69** (1) (2000)
- [Black '04] E. D. Black, A. Villar, K. Barbary, A. Bushmaker, J. Heefner, S. Kawamura, F. Kawazoe, L. Matone, S. Meidt, S. R. Rao, K. Schulz, M. Zhang and K. Libbrecht *Direct observation of broadband coating thermal noise in a suspended interferometer* Phys. Lett. **A328** (2004) 1–5
- [Brown '86] N. J. Brown *Preparation of Ultrasmooth Surfaces* Ann. Rev. Mater. Sci. **16** (1986) 371-88
- [Braginsky '03] V. B. Braginsky, M. L. Gorodetsky and S. P. Vyatchanin *Thermodynamical fluctuations in optical mirror coatings* Phys. Lett. A **312** (2003) 244–255
- [Braginsky '04] V. B. Braginsky, S. Vyatchanin, *Corner Reflectors and Quantum-Non-Demolition measurements in Gravitational-Wave Antennae* Phys. Rev. A **324** (2004) 345-360
- [Cagnoli '02] G. Cagnoli, P. Willems *Effects of nonlinear thermoelastic damping in highly stressed fibers* Phys. Rev. **B 65** (2002) 174111
- [Callen '51] H. B. Callen and T. A. Welton *Irreversibility and Generalized Noise* Phys. Rev. **83** (1951) 34–40
- [Callen '52] H. B. Callen and G. F. Greene *On a Theorem of Irreversible Thermodynamics* Phys. Rev. **86** (1952) 702–710
- [Caves 80] C. M. Caves *Quantum radiation pressure fluctuations in an interferometer* Phys. Rev. Lett. **45** (1980) 75–79

- [Chelkowski '05] S. Chelkowski, H. Vahlbruch, B. Hage, A. Franzen, N. Lastzka, K. Danzmann and R. Schnabel *Experimental characterization of frequency dependent squeezed light* Phys. Rev. A **71** (2005) 013806
- [Crooks '04] D. R. M. Crooks, G. Cagnoli, M. M. Fejer, A. Gretarsson, G. Harry, N. Nakagawa, S. Penn, R. Route, S. Rowan, P. H. Sneddon *Experimental measurements of coating mechanical loss factors* Class. Quantum Grav. **21** (2004) 1059–1066
- [Fejer '03] M. M. Fejer, S. Rowan, G. Cagnoli, D. R. M. Crooks, A. Gretarsson, G. M. Harry, J. Hough, S. D. Penn, P. H. Sneddon, and S. P. Vyatchanin, *Thermoelastic dissipation in inhomogeneous media: loss measurements and displacement noise in coated test masses for interferometric gravitational wave detectors*, Phys. Rev. D **70** (2003)
- [Giazotto '05] A. Giazotto, G. Cella, *Some Ideas on Coatingless All-Reflective ITF As* presented at the Italy-Australia Workshop on Gravitational Waves (2005).
- [Gillespie '93] A. Gillespie and F. Raab *Thermal noise in the test mass suspensions of a laser interferometer gravitational-wave detector prototype* Phys. Lett. **A 178** (1993) 357–363
- [Gillespie '94] A. Gillespie and F. Raab *Suspension loss in the pendula of laser interferometer gravitational-wave detectors* Phys. Lett. **A 190** (1994) 213–220
- [Goßler] S. Goßler, personal communication
- [Griffiths '99] D. J. Griffiths, *Introduction to Electrodynamics, 3rd Edition*, Prentice Hall, New Jersey (1999)
- [Harry '02] G. M. Harry, A. M. Gretarsson, P. R. Saulson, S. E. Kittelberger, S. D. Penn, W. J. Startin, S. Rowan, M. M. Fejer, D. R. M. Crooks, G. Cagnoli, J. Hough and N. Nakagawa *Thermal noise in interferometric gravitational wave detectors due to dielectric optical coatings* Class. Quantum Grav. **19** (2002) 897–917
- [Hudgens '98] J. W. Hudgens *Novel Miniature Spectrometer for Remote Chemical Detection* Environmental Sciences Management Program, Project ID Number 60231
- [Kajima '99] M. Kajima, N. Kusumi, S. Moriwaki, N. Mio *Wide-band measurement of mechanical thermal noise using a laser interferometer* Phys. Lett. **A 264** (1999) 251–256
- [Khalili '04] F. Ya. Khalili *Reducing the Mirrors Coating Noise in Laser Gravitational-Wave Antennae by Means of Double Mirrors* arXiv:gr-qc/0406071 (2004)
- [Levin '98] Y. Levin *Internal thermal noise in the LIGO test masses: A direct approach* Phys. Rev. D **57** (1998) 659–663
- [McKenzie '02] K. McKenzie, D. A. Shaddock, B. C. Buchler, P. K. Lam, D. E. McClelland *Experimental demonstration of a squeezing enhanced power-recycled Michelson interferometer for gravitational-wave detection* Phys. Rev. Lett. **88** (2002) 231102

-
- [McKenzie 06] K. McKenzie, M. B. Gray, S. Goßler, P. K. Lam and D. E. McClelland *Squeezed state generation for interferometric gravitational-wave detectors* Class. Quantum Grav. **23** (2006) 245–250
- [Nakagawa '02] N. Nakagawa, A. M. Gretarsson, E. K. Gustafson, and M. M. Fejer, *Thermal noise in half-infinite mirrors with nonuniform loss: A slab of excess loss in a half-infinite mirror* Phys. Rev. D **65** (2002) 102001F
- [Nieto '92] M. Nieto-Vesperinas and J. A. Sanchez-Gil *Light scattering from a random rough interface with total internal reflection* J. Opt. Sci. Am. A **9** 3 (1992) 424-436
- [Numata '03] K. Numata, M. Ando, K. Yamamoto, S. Otsuka, and K. Tsubono *Wide-Band Direct Measurement of Thermal Fluctuations in an Interferometer*. Phys. Rev. Lett. **91** (2003) 260602
- [Penn '03] S. D. Penn, P. H. Sneddon, H. Armandula, J. C. Betzwieser, G. Cagnoli, J. Camp, D. R. M. Crooks, M. M. Fejer, A. M. Gretarson, G. M. Harry, J. Hugh, S. C. Kittelberger, M. J. Mortonson, R. Route, S. Rowan and C. C. Vassiliou *Mechanical loss in tantala/silica dielectric mirror coatings* Class. Quantum Grav. **20** (2003) 2917–2928
- [Plissi '00] M. V. Plissi, C. I. Torrie, M. E. Husman, N. A. Robertson, K. A. Strain, H. Ward, H. Lück, J. Hough *GEO 600 triple pendulum suspension system: Seismic isolation and control* Rev. Sci. Instrum. **71** (2000) 2539–2545
- [Rowan '05] S. Rowan, J. Hough, D. R. M. Crooks, *Thermal Noise and Material Issues for Gravitational Wave Detectors* Phys. Lett. A **347** (2005) 25-32
- [Saleh, Teich '91] B. E. A. Saleh and M. C. Teich, *Fundamentals of Photonics*, John Wiley & Sons, Inc., New York (1991)
- [Saulson '94] Peter R. Saulson, *Fundamentals of Interferometric Gravitational Wave Detectors*, World Scientific, Singapore (1994)
- [Schiller '92] S. Schiller, I. I. Yu, M. M. Fejer, and R. L. Byer *Fused-silica monolithic total-internal-reflection resonator* Optics Letters **17** 5 (1992) 378-80
- [Shaddock '00] D. A. Shaddock, *Advanced Interferometry for Gravitational Wave Detection*, PhD thesis, Physics Department, Australian National University, Canberra, Australia (2000)
- [Siegman '86] A. E. Siegman, *Lasers*, University Science Books, Mill Valley, California (1986)
- [Vahlbruch '05] H. Vahlbruch, S. Chelkowski, B. Hage, A. Franzen, K. Danzmann and R. Schnabel *Demonstration of Squeezed-Light Enhanced Power- and Signal-recycling Michelson Interferometer* Phys. Rev. Lett. **95** (2005) 211102

- [Vahlbruch '06] H. Vahlbruch, S. Chelkowski, B. Hage, A. Franzen, K. Danzmann and R. Schnabel *Squeezed-field injection for gravitational-wave interferometers* Class. Quantum Grav. **23** (2006) 251–257
- [Willems '99] P. Willems, M. Thattai *Increased thermal noise in nonuniform fiber suspensions* Phys. Lett. **A 253** (1999) 16–20
- [Willems'02] P. Willems, V. Sannibale, J. Weel, V. Mitrofanov *Investigations of the dynamics and mechanical dissipation of a fused silica suspension* Phys. Lett. **A 297** (2002) 37–48
- [Yamamoto '01] K. Yamamoto, S. Otsuka, M. Ando, K. Kawabe, K. Tsubono *Experimental study of thermal noise caused by an inhomogeneously distributed loss* Phys. Lett. **A 280** (2001) 289–296
- [Yariv '97] A. Yariv, *Optical Electronics in Modern Communications, 5th Edition*, Oxford University Press, New York (1997)